

# Solving multi-pole challenges in the *GW*100 benchmark enables precise low-scaling *GW* calculations

Mia Schambeck,<sup>1</sup> Dorothea Golze,<sup>2</sup> and Jan Wilhelm<sup>1,\*</sup>

<sup>1</sup>*Institute of Theoretical Physics and Regensburg Center for Ultrafast Nanoscopy (RUN),  
University of Regensburg, 93053 Regensburg, Germany*

<sup>2</sup>*Faculty for Chemistry and Food Chemistry, Technische Universität Dresden, 01062 Dresden, Germany*

(Dated: June 3, 2024)

The *GW* approximation is a widely used method for computing electron addition and removal energies of molecules and solids. The computational effort of conventional *GW* algorithms increases as  $O(N^4)$  with the system size  $N$ , hindering the application of *GW* to large and complex systems. Low-scaling *GW* algorithms are currently very actively developed. Benchmark studies at the single-shot  $G_0W_0$  level indicate excellent numerical precision for frontier quasiparticle energies, with mean absolute deviations  $< 10$  meV with respect to standard implementations for the widely used *GW*100 test set. A notable challenge for low-scaling *GW* algorithms remains in achieving high precision for five molecules within the *GW*100 test set, namely  $O_3$ , BeO, MgO, BN, and CuCN, for which the deviations are in the range of several hundred meV. This is due to a spurious transfer of spectral weight from the quasiparticle to the satellite spectrum in  $G_0W_0$  calculations, resulting in multi-pole features in the self-energy and spectral function, which low-scaling algorithms fail to describe. We show in this work that including eigenvalue self-consistency in the Green's function (ev*GW*<sub>0</sub>) achieves a proper separation between satellite and quasiparticle peak, leading to a single solution of the quasiparticle equation with spectral weight close to one. ev*GW*<sub>0</sub> quasiparticle energies from low-scaling *GW* closely align with reference calculations; the mean absolute error is only 12 meV for the five molecules.

## I. INTRODUCTION

*GW* calculations [1–3] have become a standard tool for calculating electron addition and removal energies of molecules [4–6], two-dimensional materials [7–19] and solids [20–26]. Recent advancements of the *GW* method span a broad spectrum, including the application to deep core excitations [27–34], relativistic *GW* schemes [35–41], exploring excited-state potential energy surfaces from *GW*+Bethe-Salpeter [42–45], electron dynamics from Green's functions [46–57], and applying the *GW* methodology in magnetic fields [58–61]. There has also been a concerted effort towards benchmarking the accuracy of the *GW* method [62–65] and the numerical precision of *GW* implementations [5, 66–71]. An increasing number of machine learning models have emerged for predicting quasiparticle (QP) energies without performing a costly *GW* calculation [72–78]. Concerning method development beyond the *GW* approximation, vertex corrections [79–91] and connections with coupled-cluster methods [92–94] have been explored. Promising developments for the study of electronic excitations in the solid state have been also reported using coupled-cluster methods [95–101] and low-scaling Bethe-Salpeter approaches [102–104].

Despite that *GW* method development is blooming, several algorithmic bottlenecks render *GW* calculations challenging, particularly in dealing with complex or disordered systems with large simulation cells. In conventional *GW* implementations, the computational cost increases as  $O(N^4)$  with the system size  $N$ , restricting conventional *GW* calculations often to systems with a few hundred atoms [2, 72]. Various strategies have been devised to tackle this limitation, ranging from massively parallel implementations [105–111], to physically mo-

tivated approximations like embedding [112–117] and low-scaling techniques [118–131]. In this work, we focus on deterministic, low-scaling *GW* algorithms based on the *GW* space-time method by Rojas, Godby and Needs published in 1995 [118]. The *GW* space-time method relies on space-local representations and imaginary time-frequency transforms and achieves cubic scaling of the computational cost in the system size,  $O(N^3)$ , instead of quartic scaling  $O(N^4)$  of conventional *GW* algorithms. Many different techniques have been used to increase the computational efficiency of the *GW* space-time method, including pair-atomic resolution of the identity [125, 132–135], separable density fitting [124, 130, 136–140], and global resolution of the identity with a local metric [14, 123, 129, 141, 142].

All of the space-time *GW* algorithms include three Fourier transforms between imaginary time and imaginary frequency, and vice versa, which are performed numerically. This poses a significant challenge in terms of numerical precision, a challenge that has been addressed by the development of tailored imaginary-time and imaginary-frequency grids [121, 143–145]. The precision of these numerical grids has undergone rigorous benchmarking against highly accurate *GW* calculations across various systems, including solids [121, 144], two-dimensional materials [144], and molecules [70, 129, 144]. Overall, the findings indicate excellent numerical precision, typically better than 10 meV for QP energies of the highest valence states and the lowest empty states. [129, 144]

A notable challenge remains in achieving high precision for five molecules within the *GW*100 test set [5], namely  $O_3$ , BeO, MgO, BN, and CuCN [129], at the single-shot  $G_0W_0$  level of theory [2] using the Perdew-Burke-Ernzerhof (PBE) functional [146] for the underlying Kohn-Sham density functional theory [147] (KS-DFT) calculation. We refer to this procedure as  $G_0W_0@PBE$ . For these molecules, the  $G_0W_0@PBE$  energies computed from low-scaling algorithms can differ by several hundred meV from reference calcula-

\* jan.wilhelm@physik.uni-regensburg.de

tions [129]. In this work, we revisit these five molecules and we aim to demonstrate that the  $G_0W_0$ @PBE solution is unphysical and that a physical solution can be obtained using partial eigenvalue self-consistency in the Green's function or using a hybrid functional as starting point for  $G_0W_0$ . We also aim to show that the low-scaling  $GW$  algorithms are numerically precise for the  $GW$  flavors which yield a physical solution.

The article is organized as follows: We discuss the  $G_0W_0$  scheme and multi-pole artifacts in the  $GW100$  benchmark in Sec. II. We describe the low-scaling space-time  $GW$  algorithm in Sec. III and the reference  $GW$  algorithm based on contour deformation in Sec. IV. Computational details of our  $GW$  calculations are given in Sec. V. We present and discuss  $G_0W_0$ @PBE,  $evGW_0$  and  $G_0W_0$ @PBE0 calculations in Sec. VI and VII and VIII, respectively.

## II. MULTI-POLE ARTIFACTS AT THE $G_0W_0$ LEVEL

In this section, we briefly introduce the  $G_0W_0$  approach and different methods to obtain the QP solution, including the evaluation of the spectral function. We showcase the issue of multi-pole artifacts for the MgO gas phase molecule, which is part of the  $GW100$  benchmark set [5].

The  $GW100$  set is the standard molecular test set for assessing the accuracy of  $GW$  approaches and  $GW$  implementations. [31, 66, 69, 70, 87, 123, 129, 138, 148–153]  $GW100$  contains one hundred small molecules with covalent and ionic bonds covering a wide range of the periodic table. The original  $GW100$  study [5] reports the  $G_0W_0$ @PBE QP energy of the highest occupied molecular orbital (HOMO) and the lowest occupied molecular orbital (LUMO) for all one hundred molecules. Those  $G_0W_0$ @PBE data are the ones against which new low-scaling algorithms are typically benchmarked. [70, 129, 144]

A  $G_0W_0$  calculation starts from a self-consistent KS-DFT calculation [147],

$$[h_0(\mathbf{r}) + v_{xc}(\mathbf{r})]\psi_n(\mathbf{r}) = \varepsilon_n^{\text{DFT}} \psi_n(\mathbf{r}). \quad (1)$$

$h_0$  contains the kinetic energy, the Hartree potential and the external potential, while the exchange-correlation potential  $v_{xc}$  contains all electron-electron interactions beyond Hartree.  $\psi_n(\mathbf{r})$  is the KS orbital  $n$  and  $\varepsilon_n^{\text{DFT}}$  the associated KS eigenvalue. The terms  $G_0$  and  $W_0$  indicate that the Green's function  $G$  and the screened Coulomb interaction  $W$  are both computed using KS orbitals and KS eigenvalues, i.e., self-consistent updates of  $G$  and  $W$  from Green's function theory are omitted in  $G_0W_0$ .

A central object in a  $G_0W_0$  calculation is the  $G_0W_0$  correlation self-energy which can be expressed as [2, 154]

$$\Sigma_n^c(\omega) = \sum_m \sum_s \frac{\langle \psi_n \psi_m | P_s | \psi_m \psi_n \rangle}{\omega - \varepsilon_m^{\text{DFT}} + (\Omega_s - i\eta) \text{sgn}(\varepsilon_F - \varepsilon_m^{\text{DFT}})}. \quad (2)$$

Here,  $\omega$  denotes a frequency,  $\varepsilon_F$  the Fermi level of KS-DFT and  $\eta > 0$  a broadening.  $\Omega_s$  are the charge-neutral excitation energies computed using the random phase approximation, i.e. a vanishing exchange-correlation kernel [155];

$P_s$  represents the product of transition densities of the excitation  $s$ . [2, 154]

One observable computed in a  $G_0W_0$  calculation is the molecular spectral function, which takes the form of a many-body density of states [2, 156],

$$A(\omega) = \frac{1}{\pi} \text{Im} G(\omega) \text{sgn}(\varepsilon_F - \omega), \quad (3)$$

where  $G(\omega)$  is the trace over spatial arguments of the single-particle Green's function. We express the spectral function as

$$A(\omega) = \sum_n A_n(\omega), \quad (4)$$

where  $n$  runs over all KS orbitals with a contribution  $A_n(\omega)$  to the spectral function [2, 28, 121, 157]

$$\begin{aligned} A_n(\omega) &= \frac{1}{\pi} \text{Im} \frac{\text{sgn}(\omega - \varepsilon_F)}{\omega - (\varepsilon_n^{\text{DFT}} + \Sigma_n^c(\omega) + i\eta + \Sigma_n^x - v_n^{\text{xc}})} \\ &= \frac{1}{\pi} \frac{|\gamma|}{(\omega - (\varepsilon_n^{\text{DFT}} + \text{Re} \Sigma_n^c(\omega) + \Sigma_n^x - v_n^{\text{xc}}))^2 + \gamma^2}. \end{aligned} \quad (5)$$

Here,  $\gamma = \text{Im} \Sigma_n^c(\omega) + \eta$ ,  $\Sigma^x(\mathbf{r}, \mathbf{r}')$  is the exchange self-energy [2] and  $\Sigma_n^x$  and  $v_n^{\text{xc}}$  are the  $n, n$ -diagonal elements of the respective quantities.

The peak positions  $\varepsilon_n^{G_0W_0}$  of  $A(\omega)$ , known as QP energies, correspond to ionization energies and electron affinities of the molecule. QP energies are the frequencies where the real part of the denominator in Eq. (5) equals zero, i.e., the QP energies  $\varepsilon_n^{G_0W_0}$  satisfy the QP equation

$$\varepsilon_n^{G_0W_0} = \varepsilon_n^{\text{DFT}} + \text{Re} \Sigma_n^c(\varepsilon_n^{G_0W_0}) + \Sigma_n^x - v_n^{\text{xc}}. \quad (7)$$

The non-linearity of  $\Sigma_n^c(\omega)$  with respect to  $\omega$ , allows for multiple solutions  $\varepsilon_n^{G_0W_0}$  for a given level  $n$ . Such multiple solutions have been observed for five molecules in the  $GW100$  test, namely  $\text{O}_3$ ,  $\text{BeO}$ ,  $\text{MgO}$ ,  $\text{BN}$ , and  $\text{CuCN}$  at the  $G_0W_0$ @PBE level [5].

We illustrate multiple solutions of Eq. (7) for state  $n = \text{HOMO}$  of the  $\text{MgO}$  molecule, see Fig. 1 (a). The black dashed traces visualize the linear function

$$f(\omega) = \omega - (\varepsilon_{\text{HOMO}}^{\text{DFT}} + \Sigma_{\text{HOMO}}^x - v_{\text{HOMO}}^{\text{xc}}) \quad (8)$$

such that the intersections  $\varepsilon$  of  $f(\omega)$  and  $\text{Re} \Sigma_{\text{HOMO}}^c(\omega)$ ,  $f(\varepsilon) = \text{Re} \Sigma_{\text{HOMO}}^c(\varepsilon)$ , are the solutions of the QP equation (7). Five intersections are apparent,  $\varepsilon \in \{-11.00 \text{ eV}, -9.90 \text{ eV}, -7.09 \text{ eV}, -6.91 \text{ eV}, -6.68 \text{ eV}\}$ ,

where the highest solution has been picked in the original work [5] as  $G_0W_0$ @PBE HOMO energy. The large number of intersection is due to the many poles in the self-energy (2).

Each intersection  $\varepsilon$  comes with a spectral weight  $Z_\varepsilon$  that quantifies the number of electrons associated with a given peak in the spectral function.  $Z_\varepsilon$  is usually approximately computed as

$$Z_\varepsilon \approx \left[ 1 - \text{Re} \left. \frac{\partial \Sigma_n^c(\omega)}{\partial \omega} \right|_{\omega = \varepsilon} \right]^{-1}, \quad (9)$$

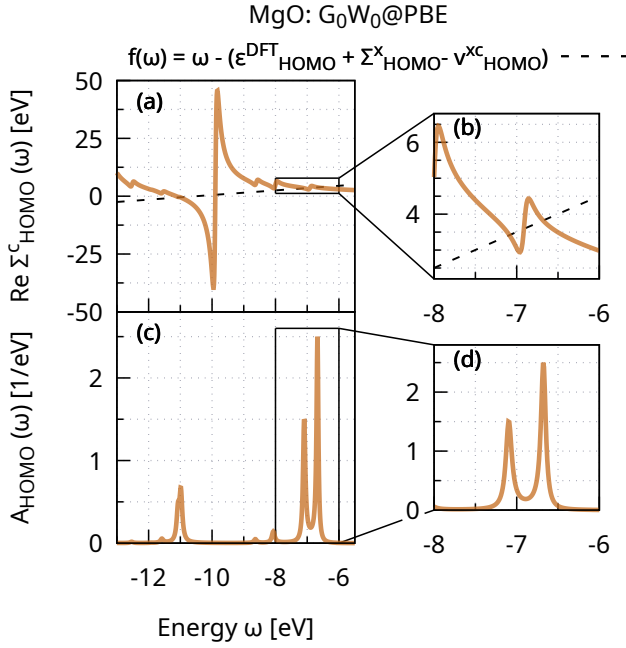


FIG. 1. (a)/(b) Real part of the  $G_0W_0@PBE$  HOMO self-energy  $\Sigma_{\text{HOMO}}^c(\omega)$ , Eq. (2) for the MgO molecule from the GW100 set. Intersections of the straight line  $f(\omega)$  and  $\text{Re}\Sigma_{\text{HOMO}}^c(\omega)$  lead to five solutions of the QP equation (7), as already discussed in Ref. 5. (c)/(d)  $G_0W_0@PBE$  HOMO contribution  $A_{\text{HOMO}}(\omega)$  to the spectral function, Eq. (5). We have computed all quantities using the numerically precise contour deformation as implemented in FHI-aims [27] and a broadening  $\eta = 1$  mHa, see further details in Sec. IV and V.

see Appendix A for a derivation. Due to the small slope of  $\Sigma_{\text{HOMO}}^c(\omega)$  at the intersections  $\varepsilon \in \{-7.09 \text{ eV}, -6.68 \text{ eV}\}$ , the associated spectral weight is large, whereas the other intersections exhibit a relatively small spectral weight. This is also apparent in the HOMO contribution  $A_{\text{HOMO}}(\omega)$  to the  $G_0W_0@PBE$  spectral function (5), see Fig. 1(c)/(d). Three major peaks are visible, precisely located at intersections of  $f(\omega)$  and  $\text{Re}\Sigma_{\text{HOMO}}^c(\omega)$ . More precisely,  $A_{\text{HOMO}}(\omega)$ , Eq. (5), features two peaks at energy  $\varepsilon \in \{-7.09 \text{ eV}, -6.68 \text{ eV}\}$  with significant spectral weight, i.e. a single QP peak is absent.

MgO is a molecule with large optical gap in the order of several eVs such that shake-up processes cannot lead to such a small splitting of peaks in  $A_{\text{HOMO}}(\omega)$ . This renders the two close peaks with similar spectral weight in  $A_{\text{HOMO}}(\omega)$  unphysical. A clear QP peak is also absent in the  $G_0W_0@PBE$  spectral function of the other four challenging molecules BeO, BN, O<sub>3</sub> and CuCN, see Fig. 5 and 6 in the appendix. Also in these cases, a single QP peak is expected. These multiple solutions are not only unphysical, but they also pose a numerical challenge to low-scaling GW algorithms [123, 129]. In this work, we address this issue.

### III. LOW-SCALING GW SPACE-TIME ALGORITHM

Many low-scaling GW algorithms [119–127, 129, 138] build on the GW space-time method [118]. In this work, we execute GW calculations using the low-scaling algorithm from Ref. 129 which adapts the space-time method for use with Gaussian basis functions. In order to introduce the basic idea of the GW space-time method, we use a generic formulation in this section for non-periodic systems projecting all quantities on real-space grids. It is important to note that this formulation differs from the original GW space-time method [118] where some quantities were calculated using a plane-wave basis set.

KS orbitals and eigenvalues are used to calculate the single-particle Green's function in imaginary time,

$$G(\mathbf{r}, \mathbf{r}', i\tau) = \begin{cases} i \sum_i^{\text{occ}} \psi_i(\mathbf{r}) \psi_i(\mathbf{r}') e^{-|(\varepsilon_i^{\text{DFT}} - \varepsilon_F)\tau|}, & \tau > 0, \\ -i \sum_a^{\text{virt}} \psi_a(\mathbf{r}) \psi_a(\mathbf{r}') e^{-|(\varepsilon_a^{\text{DFT}} - \varepsilon_F)\tau|}, & \tau < 0, \end{cases} \quad (10)$$

where the sum over the index  $i$  runs over all occupied KS orbitals and the sum over the index  $a$  over all virtual, i.e., empty KS orbitals.  $\varepsilon_F$  is the Fermi level. The irreducible polarizability follows,

$$\chi^0(\mathbf{r}, \mathbf{r}', i\tau) = -iG(\mathbf{r}, \mathbf{r}', i\tau)G(\mathbf{r}, \mathbf{r}', -i\tau), \quad (11)$$

which is then Fourier transformed to imaginary frequency,

$$\chi^0(\mathbf{r}, \mathbf{r}', i\omega) = i \int_{-\infty}^{\infty} e^{-i\omega\tau} \chi^0(\mathbf{r}, \mathbf{r}', i\tau) d\tau. \quad (12)$$

Next, the dielectric function  $\varepsilon$  can be calculated in imaginary frequency from the irreducible polarizability,

$$\varepsilon(\mathbf{r}, \mathbf{r}', i\omega) = \delta(\mathbf{r}, \mathbf{r}') - \int d\mathbf{r}'' v(\mathbf{r}, \mathbf{r}'') \chi^0(\mathbf{r}'', \mathbf{r}', i\omega), \quad (13)$$

using the Dirac delta function  $\delta(\mathbf{r}, \mathbf{r}')$  and the Coulomb interaction  $v(\mathbf{r}, \mathbf{r}') = 1/|\mathbf{r} - \mathbf{r}'|$ . The screened Coulomb interaction can be computed from the inverse dielectric function,

$$W(\mathbf{r}, \mathbf{r}', i\omega) = \int d\mathbf{r}'' \varepsilon^{-1}(\mathbf{r}, \mathbf{r}'', i\omega) v(\mathbf{r}'', \mathbf{r}'). \quad (14)$$

It is convenient in GW implementations to split the screened interaction  $W$  into the bare Coulomb interaction  $v$  and the correlation part  $W^c$ ,

$$W^c(\mathbf{r}, \mathbf{r}', i\omega) = W(\mathbf{r}, \mathbf{r}', i\omega) - v(\mathbf{r}, \mathbf{r}'). \quad (15)$$

In the space-time method,  $W^c$  is required in imaginary time,

$$W^c(\mathbf{r}, \mathbf{r}', i\tau) = \frac{i}{2\pi} \int_{-\infty}^{\infty} e^{i\omega\tau} W^c(\mathbf{r}, \mathbf{r}', i\omega) d\omega, \quad (16)$$

and the correlation self-energy is given as product of the Green's function and the screened Coulomb interaction,

$$\Sigma^c(\mathbf{r}, \mathbf{r}', i\tau) = iG(\mathbf{r}, \mathbf{r}', i\tau)W^c(\mathbf{r}, \mathbf{r}', i\tau). \quad (17)$$

The self-energy is then transformed to imaginary frequency,

$$\Sigma^c(\mathbf{r}, \mathbf{r}', i\omega) = i \int_{-\infty}^{\infty} e^{-i\omega\tau} \Sigma^c(\mathbf{r}, \mathbf{r}', i\tau) d\tau, \quad (18)$$

and we calculate its  $(n, n)$ -diagonal element,

$$\begin{aligned} \Sigma_n^c(i\omega) &= \langle \psi_n | \Sigma^c(i\omega) | \psi_n \rangle \\ &= \int d\mathbf{r} d\mathbf{r}' \psi_n(\mathbf{r}) \Sigma^c(\mathbf{r}, \mathbf{r}', i\omega) \psi_n(\mathbf{r}'). \end{aligned} \quad (19)$$

The self-energy is then analytically continued to real frequency, i.e. we determine the fit parameters  $a_{j,n}$  and  $b_{j,n}$  of an  $N$ -parameter Padé approximant  $P_n(i\omega)$  [5, 158] to match  $\Sigma_n^c(i\omega)$  of QP level  $n$  as closely as possible,

$$\Sigma_n^c(i\omega) \approx P_n(i\omega) = \frac{\sum_{j=1}^{(N-1)/2} a_{j,n} \cdot (i\omega)^j}{1 + \sum_{j=1}^{N/2} b_{j,n} \cdot (i\omega)^j}. \quad (20)$$

Based on the identity theorem for analytic functions, one evaluates  $P_n$  at real frequencies to compute the self-energy at real frequencies,  $\Sigma_n^c(\omega) \approx P_n(\omega)$ . [2, 5]

Focusing on the  $G_0W_0$  method already introduced before, we use KS orbitals to approximate the QP wavefunctions and we compute  $G$  and  $W$  only once using KS orbitals and KS eigenvalues from Eqs. (10)–(14). The QP energies  $\epsilon_n^{G_0W_0}$  can finally be calculated by solving the QP equation (7).

In this work, we also employ  $evGW_0$  where  $W$  is fixed at the  $G_0W_0$  level, while  $G$  in Eq. (17) is recomputed from Eq. (10) using the QP energies (7). This procedure is repeated until self-consistency in the QP energies is reached. [2]

The computational cost of the presented algorithm increases with  $O(N^3)$  in the system size  $N$ . This is apparent from Eq. (10), which requires  $O(N_{\text{grid}}^2(N_{\text{occ}} + N_{\text{vir}})) = O(N^3)$  number of floating point operations, where  $N_{\text{grid}}$  is the number of real-space grid points,  $N_{\text{occ}}$  the number of occupied KS orbitals, and  $N_{\text{vir}}$  the number of virtual KS orbitals.

In a standard  $GW$  algorithm, a computational bottleneck is evaluating the Adler-Wiser formula [159, 160] for the irreducible polarizability in imaginary frequency,

$$\chi^0(\mathbf{r}, \mathbf{r}', i\omega) = \sum_i^{\text{occ}} \sum_a^{\text{virt}} \frac{2(\epsilon_i - \epsilon_a)}{(\epsilon_i - \epsilon_a)^2 + \omega^2} \psi_i(\mathbf{r}) \psi_a(\mathbf{r}) \psi_i(\mathbf{r}') \psi_a(\mathbf{r}'). \quad (21)$$

This computation requires  $O(N_{\text{grid}}^2 N_{\text{occ}} N_{\text{virt}}) = O(N^4)$  operations, and is thus computationally more demanding than the whole low-scaling algorithm (10)–(18) for a large system.

The drawback of algorithm (10)–(18) is that it requires very fine real-space grids, in particular when evaluating Coulomb interactions in Eq. (13) and (14). This is why the original  $GW$  space-time method [118] used a plane-waves basis for the calculation of  $\epsilon(i\omega)$  and  $W(i\omega)$ . Then, the  $O(N^3)$ -scaling convolutions (13) and (14) in real space transform into  $O(N^2)$  multiplications in the plane-wave basis. The inversion of  $\epsilon(i\omega)$  remains as cubic-scaling step. For the low-scaling

$GW$  implementation used in this work [129], Eq. (10)–(18) have been reformulated in a Gaussian basis set resulting in effective  $O(N^2)$  scaling [123, 129].

#### IV. REFERENCE $GW$ CALCULATIONS WITH CONTOUR DEFORMATION

In the low-scaling  $GW$  space-time method, one major challenge regarding numerical precision is the analytic continuation of  $\Sigma^c(i\omega)$  to  $\Sigma^c(\omega)$ . A numerically more precise procedure for computing  $\Sigma^c(\omega)$  is the contour deformation (CD) [2, 27, 161–163]. The starting point of CD is Eq. (17), formulated in real frequency, [2]

$$\Sigma^c(\mathbf{r}, \mathbf{r}', \omega) = \frac{i}{2\pi} \int_{-\infty}^{\infty} G(\mathbf{r}, \mathbf{r}', \omega + \omega') W^c(\mathbf{r}, \mathbf{r}', \omega') d\omega'. \quad (22)$$

Due to the pole structure of  $G$  and  $W$  on the real-frequency axis, the numerical integration of Eq. (22) is potentially unstable [2]. One way to circumvent this problem is to rewrite Eq. (22) with a contour integral,

$$\begin{aligned} \Sigma^c(\mathbf{r}, \mathbf{r}', \omega) &= \frac{i}{2\pi} \oint d\omega' G(\mathbf{r}, \mathbf{r}', \omega + \omega') W^c(\mathbf{r}, \mathbf{r}', \omega') \\ &\quad - \frac{1}{2\pi} \int_{-\infty}^{\infty} d\omega' G(\mathbf{r}, \mathbf{r}', \omega + i\omega') W^c(\mathbf{r}, \mathbf{r}', i\omega'), \end{aligned} \quad (23)$$

where the closed integral comprises the real axis, two arcs and the imaginary axis. The closed integral can be calculated using Cauchy's residue theorem, while the imaginary axis can be integrated numerically since the problematic pole structure of  $G$  and  $W$  is restricted to the real frequency axis. [2] QP energies from CD follow from solving the QP equation (7).

The scaling for evaluating the self-energy from CD is  $O(N^4)$  for a single valence excitation [27], which is an order higher than the  $O(N^3)$ -scaling of the  $GW$  space-time method. CD is numerically highly accurate. It was shown that CD reproduces the exact self-energy structure by comparing with fully analytic solutions obtained by evaluating Eq. (2). [27] We use therefore the CD approach as reference to assess the numerical precision of our low-scaling  $GW$  algorithm. More details on CD can be found in Refs. 2 and 27.

#### V. COMPUTATIONAL DETAILS

##### A. Low-scaling $GW$ calculations using CP2K

The low-scaling  $GW$  space-time algorithm used in this work [129] is implemented in the CP2K software package [164, 165]. CP2K employs a Gaussian basis set for representing KS orbitals. We use the Gaussian and augmented plane-waves scheme (GAPW) [166] in CP2K which allows for all-electron calculations. The low-scaling  $G_0W_0$  implementation [129] is a reformulation of the space-time

method [118] in a Gaussian basis set, where sparsity is introduced by combining a global resolution-of-the-identity (RI) scheme with a truncated Coulomb metric [141, 142].

For expanding KS orbitals, we use the def2-QZVP basis set [167] with an RI-cc-pV5Z auxiliary basis [168]. We choose a minimax time-frequency grid [121, 143, 144, 169] with 30 points for all low-scaling  $GW$  calculations. For the RI with the truncated Coulomb metric we set a truncation radius of 3 Å [141, 142]. We compute two- and three-center integrals over Gaussians using recursive, analytical schemes [170, 171]. The self-energy is analytically continued from imaginary frequency to the real frequency using a Padé model [5, 158] with 16 parameters. We broaden the spectral functions using  $\eta = 1 \text{ mHa} = 27.2 \text{ meV}$  in Eq. (5).

### B. Reference $GW$ calculations with contour deformation using FHI-aims

We use the CD- $GW$  algorithm [27] as implemented in the FHI-aims software package [172]. FHI-aims is an all-electron electronic structure code using numerical atom-centered orbitals (NAO) for expanding KS orbitals [172]. We use the Gaussian def2-QZVP [167] basis set, which can be also represented as NAO basis, and an automatically generated RI basis set. In the CD, we employ a modified Gauss-Legendre grid [173] for the evaluation of the imaginary-frequency integral term, setting the number of frequency points to 2000 to obtain benchmark quality. The broadening parameter [27] is set to a rather large value  $\eta = 4 \text{ mHa} = 108.8 \text{ meV}$  to facilitate the convergence in the  $evGW_0$  case. The only exception is that for Fig. 1, we use a smaller broadening of 1 mHa to obtain sharp and well-separated peaks in the spectral function. The broadening of peaks in the spectral function resulting from CD differs from that of analytic continuation, as outlined in Ref. 27. Therefore it is difficult to directly compare peak widths and heights in the spectral function between CD and analytic continuation.

## VI. LOW-SCALING $G_0W_0@PBE$ CALCULATIONS ON $O_3$ , $BeO$ , $MgO$ , $BN$ , $CuCN$

In this section we present low-scaling  $G_0W_0@PBE$  calculations on the five molecules,  $O_3$ ,  $BeO$ ,  $MgO$ ,  $BN$ , and  $CuCN$ , and we will discuss the challenges that occurred.

It was already observed in the original  $GW100$  work [5] that computing the  $G_0W_0@PBE$  HOMO energy of  $O_3$ ,  $BeO$ ,  $MgO$ ,  $BN$ , and  $CuCN$  posed a significant numerical challenge. In the analytic continuation, this challenge was addressed by employing a 128-pole function to fit  $\Sigma_{HOMO}^c(i\omega)$  for obtaining  $\Sigma_{HOMO}^c(\omega)$  along the real-frequency axis. This high-precision fit was essential for accurately computing the  $G_0W_0@PBE$  HOMO energy from the QP equation (7) for the five aforementioned molecules. For all other 95 molecules, a 16-pole fit on  $\Sigma_{HOMO}^c$  was sufficient for accurately computing the  $G_0W_0@PBE$  HOMO energy.

$GW$  space-time algorithms require in general three Fourier transforms between imaginary time and imaginary frequency, as discussed in Sec. III. These transforms are executed numerically using discrete time and frequency grids. The functions in imaginary time and frequency usually have long tails and localized features. The usual Fast Fourier Transform with homogeneously spaced integration grids would need a large number of discrete time or frequency points. Instead, a non-equidistant Fourier transform can reduce the number of time and frequency points drastically [121, 144]. Non-equidistant grids can be set up through various techniques aimed at identifying discrete points that are optimal in a certain sense. Such approaches include the minimax approximation [121, 123, 129, 143, 144, 174–177] or least-square quadratures [125, 178–182]. Both algorithms have in common that they are numerically ill-conditioned and grid generation is typically restricted to less than 100 grid points. For instance, the recently introduced GreenX library [143] offers minimax time and frequency grids, each containing up to 34 points [143, 144, 183]. Consequently, when utilizing time and frequency grids from the GreenX library, the number of parameters available for fitting  $\Sigma^c(i\omega)$  is limited to 34. This is not sufficient for accurately computing the  $G_0W_0@PBE$  HOMO energy of the five challenging molecules,  $O_3$ ,  $BeO$ ,  $MgO$ ,  $BN$ ,  $CuCN$ , [123, 129, 144] which required a fit with a 128-pole model [5], that requires at least 128 imaginary-frequency points.

We now use our low-scaling  $GW$  implementation [129] to compute the  $G_0W_0@PBE$  self-energy and spectral function. The results for the  $MgO$  molecule are shown as violet traces in Fig. 2(a) and (c). Low-scaling  $GW$  [129] fails to reproduce the shallow self-energy pole at  $\omega \approx -7.0 \text{ eV}$  [Fig. 2(a) and zoom in Fig. 1(b)] which results in a single peak of the spectral function at  $\omega \approx -7.0 \text{ eV}$  [Fig. 2(c)] instead of the split peak present in the reference CD calculation [Fig. 2(c)]. The same failure in computing the self-energy has been observed in the original work, Ref. 5 (Fig. 13), when using analytical continuation with a 16-pole approximant to the self-energy. When using a 128-pole approximant for analytical continuation all poles of the self-energy were correctly reproduced [5]. The low-scaling  $GW$  implementation [129] is currently restricted to at most 34 imaginary-frequency points, and thus 34 fit parameters for analytic continuation. The Padé model is thus not flexible enough to accurately reproduce the  $G_0W_0@PBE$  self-energy matrix elements for the HOMO of  $MgO$ . The same observation is made for  $O_3$ ,  $BeO$ ,  $BN$ , and  $CuCN$  (Fig. 6 in the appendix).

As discussed in Sec. II, the multiple solutions at the  $G_0W_0@PBE$  level of theory are an artifact. It was found that the erroneous multisolution behavior at the  $G_0W_0@PBE$  level becomes increasingly pronounced with higher binding energies of the occupied states. Most notably, it has been observed that  $G_0W_0@PBE$  generally fails to reproduce a unique QP solution for molecular 1s core states. [28] The failure was traced back to an extreme transfer of spectral weight from the QP peak to the satellite spectrum. It was shown that the correct physics, a single QP peak for core states, can be restored by using eigenvalue self-consistent schemes, renormalized sin-

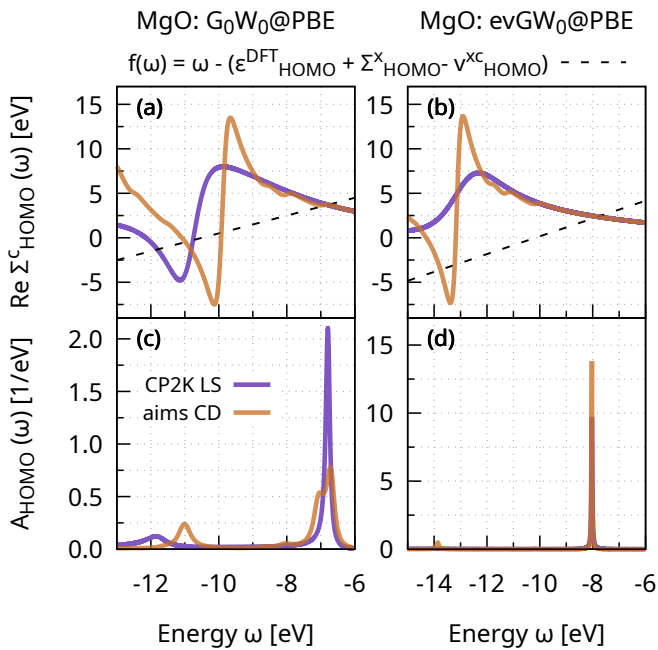


FIG. 2. Real part of the HOMO self-energy  $\Sigma_{\text{HOMO}}^c(\omega)$  [ $G_0W_0$ @PBE in (a) and  $evGW_0$ @PBE in (b)] and the HOMO contribution to the spectral function  $A_{\text{HOMO}}(\omega)$  [Eq. (5),  $G_0W_0$ @PBE in (c) and  $evGW_0$ @PBE in (d)] for the molecule MgO; computed from low-scaling  $GW$  in the CP2K package [129] ("CP2K LS"; violet traces) and from the highly accurate CD as implemented in FHI-aims [27] ("aims CD"; brown traces).  $\Sigma_{\text{HOMO}}^c(\omega)$  and  $A(\omega)$  for the other four numerically challenging molecules BeO,  $O_3$ , BN, CuCN from the  $GW_{100}$  test set [5] are available in Figs. 6 and 7 for  $G_0W_0$ @PBE and  $evGW_0$ @PBE in the appendix.

gles or by using  $G_0W_0$  with hybrid functionals with almost 50 % of exact exchange as a starting point. [28, 33] The best quantitative results with respect to experiment were obtained with  $evGW_0$ @PBE or a Hedin shift in the Green's function, which can be viewed as an approximation of  $evGW_0$ . [33]

## VII. NUMERICALLY PRECISE LOW-SCALING $evGW_0$ CALCULATIONS ON $O_3$ , BeO, MgO, BN, CuCN

Motivated by the studies on core levels [27, 28, 33], we explore  $evGW_0$  aiming to restore proper QP peaks in the spectral function of the five molecules  $O_3$ , BeO, MgO, BN, CuCN. The spectral function  $A_{\text{HOMO}}$  for the MgO molecule at the  $evGW_0$ @PBE level is shown in Fig. 2(d). Only a single QP peak in the spectral function is present at  $\omega = 8.03$  eV. The QP peak computed from the low-scaling algorithm [129] and the CD [27] match in position (within 9 meV) and spectral weight (within 1 %, Table I).

We investigate the drastic difference between the spectral function computed with  $G_0W_0$  and  $evGW_0$  by inspecting the respective self-energies, Fig. 2(a) and (b). For the  $evGW_0$  self-energy [Fig. 2(b)] the poles are shifted by  $\sim 2$  eV towards lower energy compared to the  $G_0W_0$  self-energy [Fig. 2(a)].

	$O_3$	BeO	MgO	BN	CuCN
$ \epsilon_{\text{HOMO}}^{evGW_0@PBE} $ (CD)	12.667	10.141	8.039	11.695	10.663
$ \epsilon_{\text{HOMO}}^{evGW_0@PBE} $ (LS)	12.649	10.134	8.030	11.685	10.649
$Z_{\text{HOMO}}$ (CD)	0.83	0.85	0.68	0.85	0.79
$Z_{\text{HOMO}}$ (LS)	0.88	0.78	0.68	0.85	0.80

TABLE I.  $evGW_0$ @PBE HOMO energy,  $\epsilon_{\text{HOMO}}^{evGW_0@PBE}$  and spectral weight  $Z_{\text{HOMO}}$  of the HOMO peak, computed from CD [27] and from low-scaling (LS)  $GW$  [129] for the five difficult molecules from the  $GW_{100}$  set using a def2-QZVP basis set. The spectral weight  $Z$  has been computed according to Eq. (A4).

The consequence is that there is only a single crossing point of the self-energy and the dashed straight line  $f(\omega)$ , Eq. (8), close to  $\omega = 8.03$  eV. The slope of the self-energy is small at this crossing point such that the associated spectral weight is close to one.

As discussed for core-levels [28], shifting the poles of the self-energy towards lower energies, conveys to shifting the satellite spectrum away from the QP peak. Satellites are due to multielectron excitations, i.e., a charged electron or hole excitation couples to further charge-neutral electronic excitations. Satellites are found at more negative frequencies than the QP peak and correlate to pole features in the real part of the self-energy or, equivalently, peaks in the imaginary part of  $\Sigma^c$ . A large  $\text{Im}\Sigma^c$  results in low spectral weights, i.e., satellite character as obvious from Eq. (6). Poles in the self-energy occur at  $\epsilon_i^{\text{DFT}} - \Omega_s$  and  $\epsilon_a^{\text{DFT}} + \Omega$ , where  $i$  denotes an occupied and  $a$  an unoccupied state, see Eq. (2). The poles relevant for the discussion are the ones at  $\epsilon_{\text{HOMO}}^{\text{DFT}} - \Omega_s$ . At the  $G_0W_0$ @PBE level,  $\epsilon_{\text{HOMO}}^{\text{DFT}}$  is the PBE eigenvalue, which is overestimated by a few electron volts. The  $\Omega_s$  values are close to PBE eigenvalue differences and thus underestimated. Consequently, the poles  $\epsilon_{\text{HOMO}}^{\text{DFT}} - \Omega_s$  occur at too high frequencies and are generally too close to the QP excitation. For HOMO excitations, the satellite and the QP excitations are in most cases still well separated. However, in the MgO case, the satellite and the QP solution get so close that spectral weight is transferred from the QP peak to the satellite, resulting in a multisolution behavior.

When using  $evGW_0$ @PBE, the PBE eigenvalues in  $G$  are replaced by  $\epsilon_m^{\text{DFT}} + \Delta\epsilon_m$ , where  $\Delta\epsilon_m$  is the  $evGW_0$  correction. Since  $\Delta\epsilon_{\text{HOMO}}$  is negative, the poles  $\epsilon_{\text{HOMO}}^{\text{DFT}} + \Delta\epsilon_{\text{HOMO}} - \Omega_s$  shift to more negative frequencies, achieving a proper separation between satellite and QP peak. The same is observed for the other four molecules (Fig. 7 in the appendix).

We report the total spectral function  $A(\omega)$  for all five challenging molecules,  $O_3$ , BeO, MgO, BN, CuCN, from  $evGW_0$  in Fig. 3. For all molecules, the HOMO peak positions of low-scaling  $GW$  [129] and CD [27] agree well, the mean absolute deviation is only 12 meV (Table I). The width of the QP peaks differ between low-scaling  $GW$  and the CD; the reason is the inherently different definition of the broadening parameter  $\eta$  in the two algorithms, cf. Eq. (5) and Ref. 27.

Our work shows that low-scaling space-time  $evGW_0$ @PBE is numerically precise for  $O_3$ , BeO, MgO, BN, CuCN. The

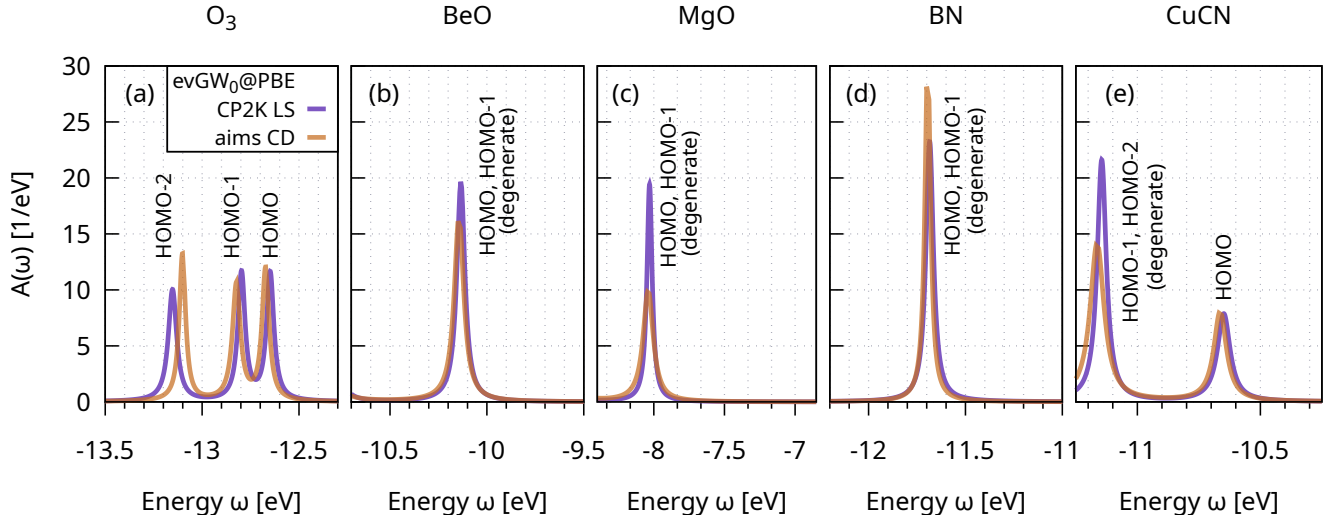


FIG. 3. (a)-(e)  $evGW_0@PBE$  spectral function for five numerically challenging molecules ( $O_3$ ,  $BeO$ ,  $MgO$ ,  $BN$ ,  $CuCN$ ) computed from low-scaling  $GW$  [129] (CP2K LS) and from CD [27] (aims CD). Peak positions and spectral weight of the HOMO peaks are listed in Table I.  $G_0W_0@PBE$  and  $G_0W_0@PBE0$  spectral functions are shown in Fig. 4 and 5. Graphical solutions of the QP equation (7) are also shown in the appendix, Fig. 6, 7 and 8 for  $G_0W_0@PBE$ ,  $evGW_0@PBE$ , and  $G_0W_0@PBE0$ , respectively.

improvement compared to the  $G_0W_0@PBE$  is due to the fact that  $evGW_0@PBE$  yields well-defined QP valence peaks, whereas  $G_0W_0@PBE$  fails to produce a physical result. Therefore, it is not reasonable to invest effort in developing low-scaling  $GW$  methods which can recover the  $G_0W_0@PBE$  solution for these five molecules, as it is an insufficient level of theory from the outset. Also, when comparing to experimental bandgaps, the  $evGW_0$  scheme is generally recommended over  $G_0W_0$  [2, 82]. The enhanced computational cost of  $evGW_0$  over  $G_0W_0$  might be reduced again by using Hedin shifts [33, 184].

### VIII. NUMERICALLY PRECISE LOW-SCALING $G_0W_0@PBE0$ CALCULATIONS ON $O_3$ , $BeO$ , $MgO$ , $BN$ , $CuCN$

We also compute the HOMO QP energy at the  $G_0W_0@PBE0$  level, see Table II. The low-scaling algorithm reproduces the QP energies from CD within 9 meV and the spectral weights within 0.01. The total spectral functions  $A(\omega)$  displayed in Fig. 5 follows also closely the CD reference. This is because the poles in the real part of  $\Sigma_{HOMO}^c$  shift by 2–3 eV to more negative frequencies (Fig. 8 in the appendix), similarly to  $evGW_0@PBE$ , which is due to the fact that  $\epsilon_{HOMO}^{DFT}$  is more negative at the PBE0 than the PBE level. The pole positions  $\epsilon_{HOMO}^{DFT} - \Omega_s$  are thus moving to the left on our energy scale. A proper separation between satellite and QP peak is consequently also achieved at the  $G_0W_0@PBE0$  level and we obtain also a unique QP solution for all five molecules. This confirms the observation from our  $evGW_0@PBE$  study from Sec. VII: our low-scaling  $GW$  algorithm [129] is numerically precise if the correct physics is restored and a well-defined QP peak is obtained.

### IX. CONCLUSION

In summary, our study revisits low-scaling  $GW$  calculations on molecules  $O_3$ ,  $BeO$ ,  $MgO$ ,  $BN$ , and  $CuCN$  from the  $GW100$  benchmark set. Previous studies [129, 144] encountered numerical challenges, particularly with the computation of the  $G_0W_0@PBE$  HOMO energy for these molecules from low-scaling  $GW$ . These challenges arise from the presence of unphysical multiple solutions of the quasiparticle equation at the  $G_0W_0@PBE$  level, which can be traced back to an in-

	$O_3$	$BeO$	$MgO$	$BN$	$CuCN$
$ \epsilon_{HOMO}^{G_0W_0@PBE0} $ (CD)	12.566	9.646	7.459	11.545	10.253
$ \epsilon_{HOMO}^{G_0W_0@PBE0} $ (LS)	12.557	9.643	7.454	11.542	10.230
$Z_{HOMO}$ (CD)	0.81	0.76	0.67	0.83	0.81
$Z_{HOMO}$ (LS)	0.81	0.77	0.67	0.83	0.81

TABLE II.  $G_0W_0@PBE0$  HOMO energy,  $\epsilon_{HOMO}^{G_0W_0@PBE0}$  and spectral weight  $Z_{HOMO}$  of the HOMO peak, computed from CD [27] and from low-scaling (LS)  $GW$  [129] for all five difficult molecules from the  $GW100$  set using a def2-QZVP basis set. The spectral weight  $Z$  has been computed according to Eq. (A4).

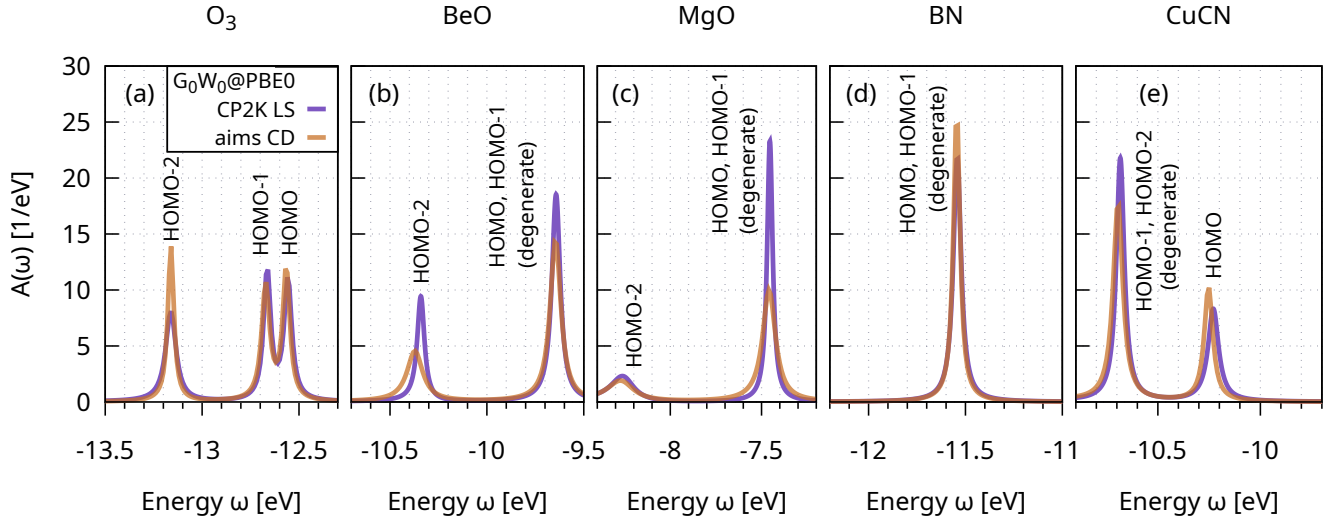


FIG. 4. (a)-(e)  $G_0W_0@PBE0$  spectral function for  $O_3$ , BeO, MgO, BN, CuCN computed from low-scaling  $GW$  in CP2K [129] (CP2K LS) and from CD in FHI-aims [27] (aims CD).

sufficient separation between quasiparticle peak and satellite positions. Applying self-consistency in the Green's function ( $evGW_0$ ) or using a hybrid functional as starting point for the  $G_0W_0$  calculation restores the correct separation between QP peak and satellite. This leads to a single HOMO QP peak and small satellites weights. Low-scaling  $GW$  computations yield numerically precise HOMO energies of  $O_3$ , BeO, MgO, BN, and CuCN, with a mean absolute deviation in the order of only 10 meV from reference calculations with CD for  $GW$  flavors which produce a physical result.

#### DATA AVAILABILITY

Inputs and outputs of all calculations reported in this work are available in a NOMAD repository [185] and in a Github repository [186]. The low-scaling  $GW$  algorithm [129] used in this work is available in the open-source package CP2K [164, 165].

#### ACKNOWLEDGMENTS

We acknowledge funding by the Barcelona Supercomputing Center via the 2023 Call for Inno4Scale Innovation Studies, project Exa4GW, Inno4scale-202301-036. D.G. and J.W. acknowledge the Deutsche Forschungsgemeinschaft (DFG, German Research Foundation) for funding via the Emmy Noether Programme (Project No. 453275048 and 503985532, respectively). The authors gratefully acknowledge the computing time provided to them on the high performance computer Noctua 2 at the NHR Center PC2. These are funded by the Federal Ministry of Education and Research and the state governments participating on the basis of the resolutions of the GWK for the national high-performance computing at universities ([www.nhr-verein.de/unsere-partner](http://www.nhr-verein.de/unsere-partner)).

## APPENDIX

### Appendix A: Spectral function and spectral weight

In this appendix, we derive Eq. (9) for the spectral weight  $Z_\epsilon$  associated with a peak at energy  $\epsilon$  of the spectral function. The spectral weight is the integral of that peak of  $A_n(\omega)$ ,

$$Z_\epsilon = \int_{\epsilon-\Delta}^{\epsilon+\Delta} A_n(\omega) d\omega \quad (\text{A1})$$

$$= \int_{\epsilon-\Delta}^{\epsilon+\Delta} \frac{1}{\pi} \frac{|\gamma|}{(\omega - (\epsilon + \text{Re}(\Sigma_n^c(\omega) - \Sigma_n^c(\epsilon)))^2 + |\gamma|^2)} d\omega. \quad (\text{A2})$$

We use  $\gamma = \text{Im} \Sigma_n^c(\omega) + \eta$  and we integrate over the interval  $[\epsilon - \Delta, \epsilon + \Delta]$  with a parameter  $\Delta$  to exclude other peaks from the integration. We have used Eq. (5) and the QP equation (7) to arrive at the denominator in Eq. (A2).

To evaluate the integral (A2), we assume that  $\text{Im} \Sigma_n^c(\omega)$  is independent of frequency and we use Taylor expansion of  $\text{Re} \Sigma_n^c(\omega)$  around  $\omega = \epsilon$ ,

$$\text{Re} [\Sigma_n^c(\omega) - \Sigma_n^c(\epsilon)] \approx \text{Re} \left. \frac{\partial \Sigma_n^c(\omega)}{\partial \omega} \right|_{\omega = \epsilon} \cdot (\omega - \epsilon). \quad (\text{A3})$$

Carrying out the integration (A2) gives the common approximate expression for the spectral weight,

$$Z_\epsilon \approx \left[ 1 - \text{Re} \left. \frac{\partial \Sigma_n^c(\omega)}{\partial \omega} \right|_{\omega = \epsilon} \right]^{-1}.$$

In practice, for Table I and II, we determine the spectral weight  $Z$  of a peak in  $A(\omega)$  by fitting a Lorentz function

$$L(\omega) = Z \cdot \frac{1}{\pi} \frac{\gamma}{(\omega - \epsilon_n^{G_0W_0})^2 + \gamma^2} \quad (\text{A4})$$



to the spectral function  $A(\omega)$ . We fix the position of the peak as the solution of the QP equation  $\epsilon_n^{G_0W_0}$ , while the peak width  $\gamma$  and the spectral weight  $Z$  were fitted.

### Appendix B: Self-energy and spectral function of all molecules O<sub>3</sub>, BeO, MgO, BN, CuCN

We provide spectral function  $A(\omega)$  of the previously challenging five molecules O<sub>3</sub>, BeO, MgO, BN, CuCN computed from  $G_0W_0@PBE$  (Fig. 5). We also show  $\text{Re}(\Sigma_{\text{HOMO}}^c)$ ,  $\text{Im}(\Sigma_{\text{HOMO}}^c)$  and  $A_{\text{HOMO}}$  [Eq. (5)] for O<sub>3</sub>, BeO, MgO, BN and CuCN computed from  $G_0W_0@PBE$ ,  $evGW_0@PBE$  and  $G_0W_0@PBE0$  (Fig. 6, 7 and 8).

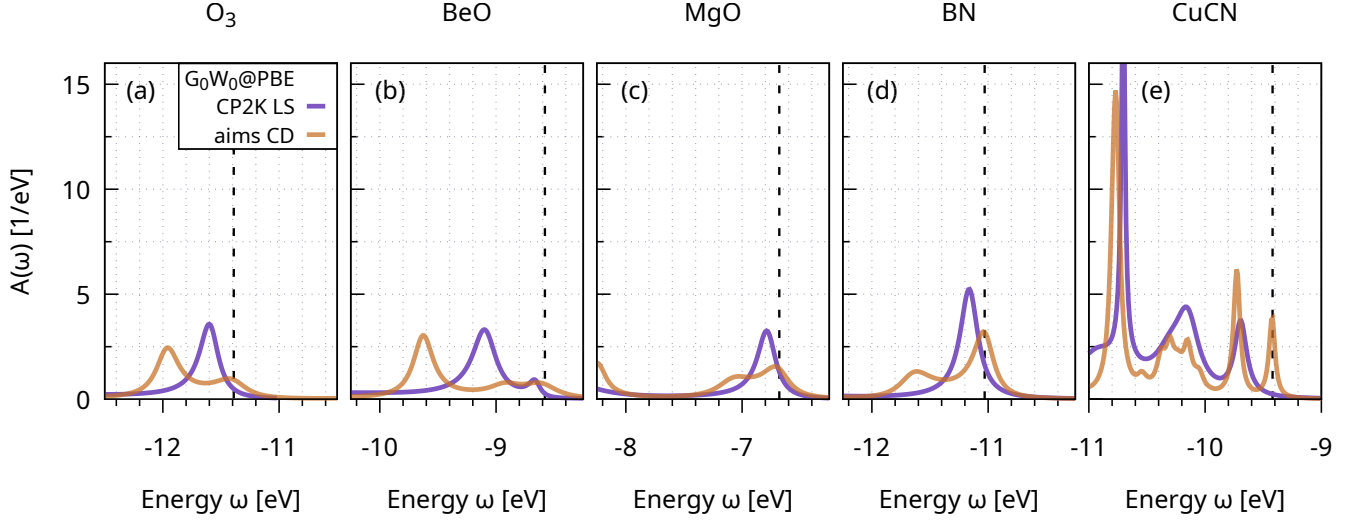


FIG. 5. (a)-(e)  $G_0W_0@PBE$  spectral function for  $O_3$ , BeO, MgO, BN, CuCN computed from low-scaling GW in CP2K [129] (CP2K LS) and from CD in FHI-aims [27] (aims CD). The dashed lines indicate the  $G_0W_0@PBE$  HOMO energy computed from FHI-aims and 128-parameter Padé continuation taken from the original GW100 work [5].

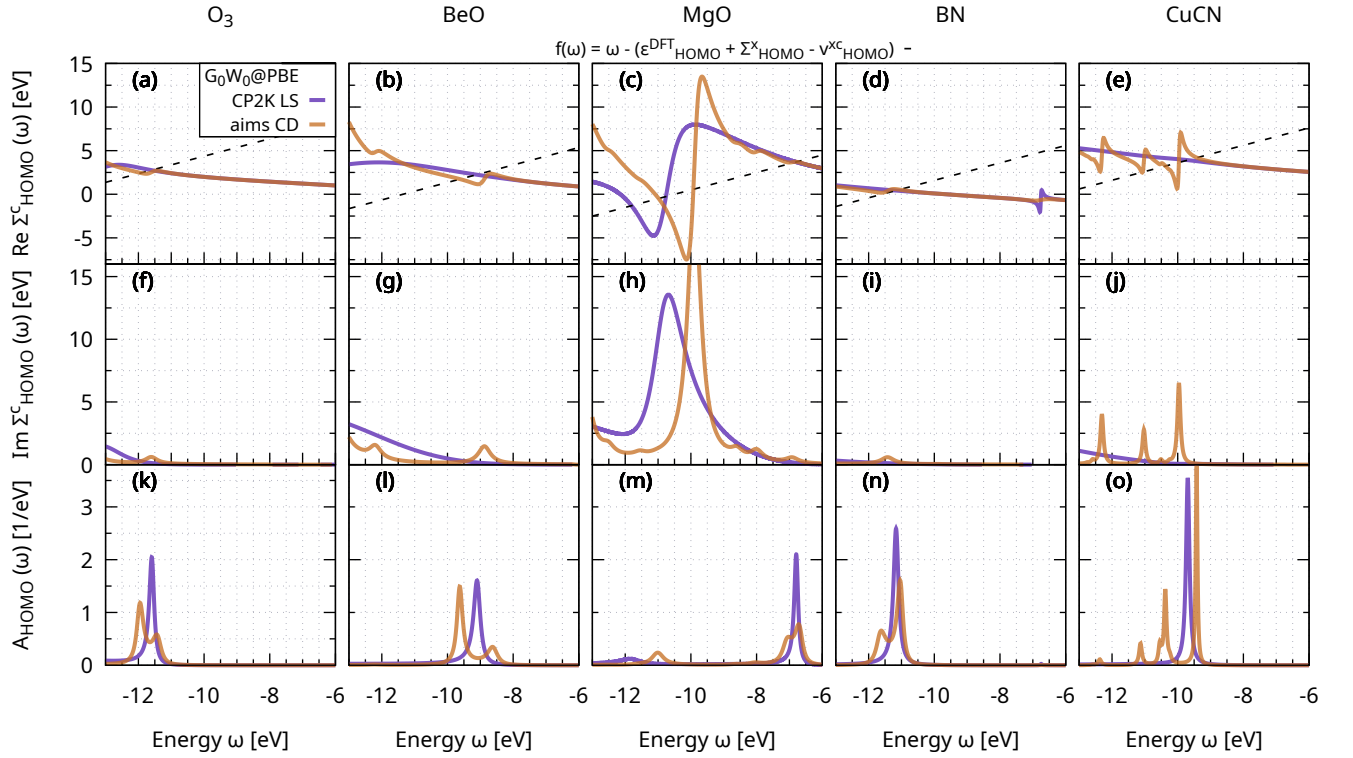


FIG. 6. (a)-(e)  $\text{Re}(\Sigma_{\text{HOMO}}^{\text{C}})$ , (f)-(j)  $\text{Im}(\Sigma_{\text{HOMO}}^{\text{C}})$ , (k)-(o)  $A_{\text{HOMO}}$  [Eq. (5)] for  $O_3$ , BeO, MgO, BN and CuCN computed from  $G_0W_0@PBE$ .

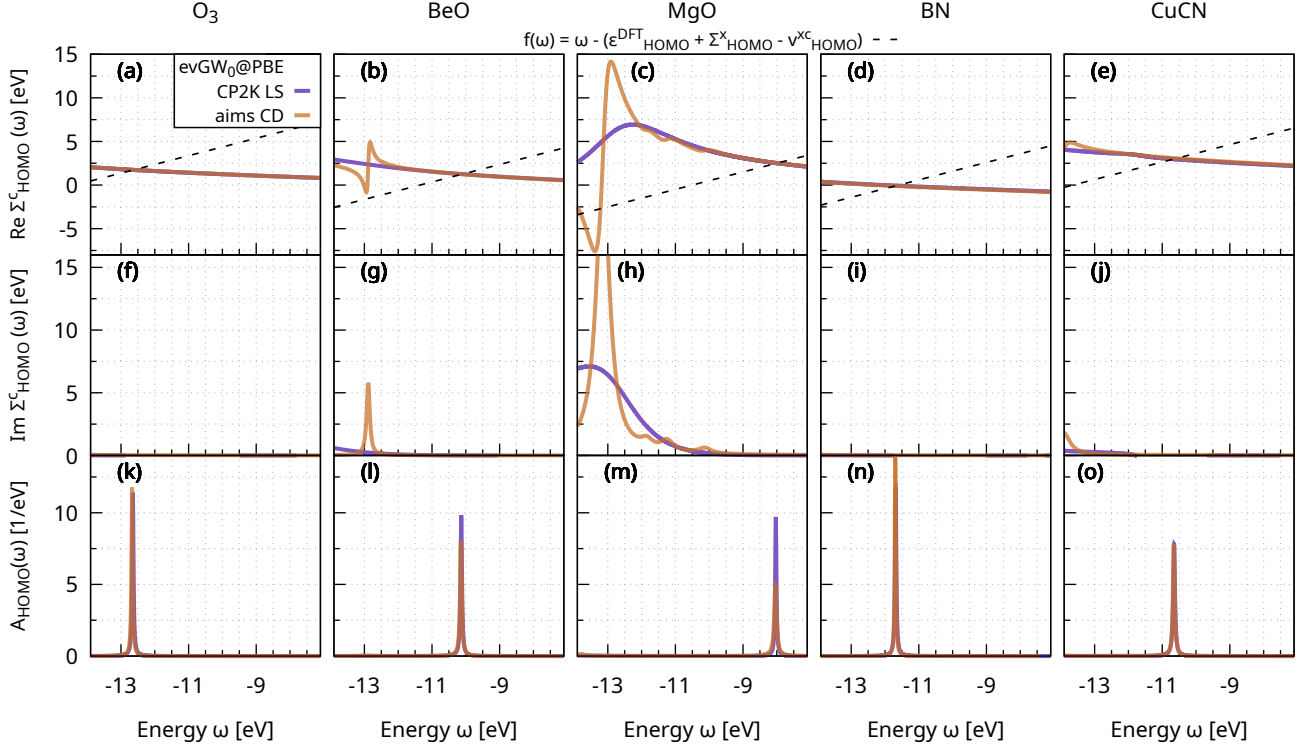


FIG. 7. (a)-(e)  $\text{Re}(\Sigma_{\text{HOMO}}^c)$ , (f)-(j)  $\text{Im}(\Sigma_{\text{HOMO}}^c)$ , (k)-(o)  $A_{\text{HOMO}}$  [Eq. (5)] for O<sub>3</sub>, BeO, MgO, BN and CuCN computed from evGW<sub>0</sub>@PBE.

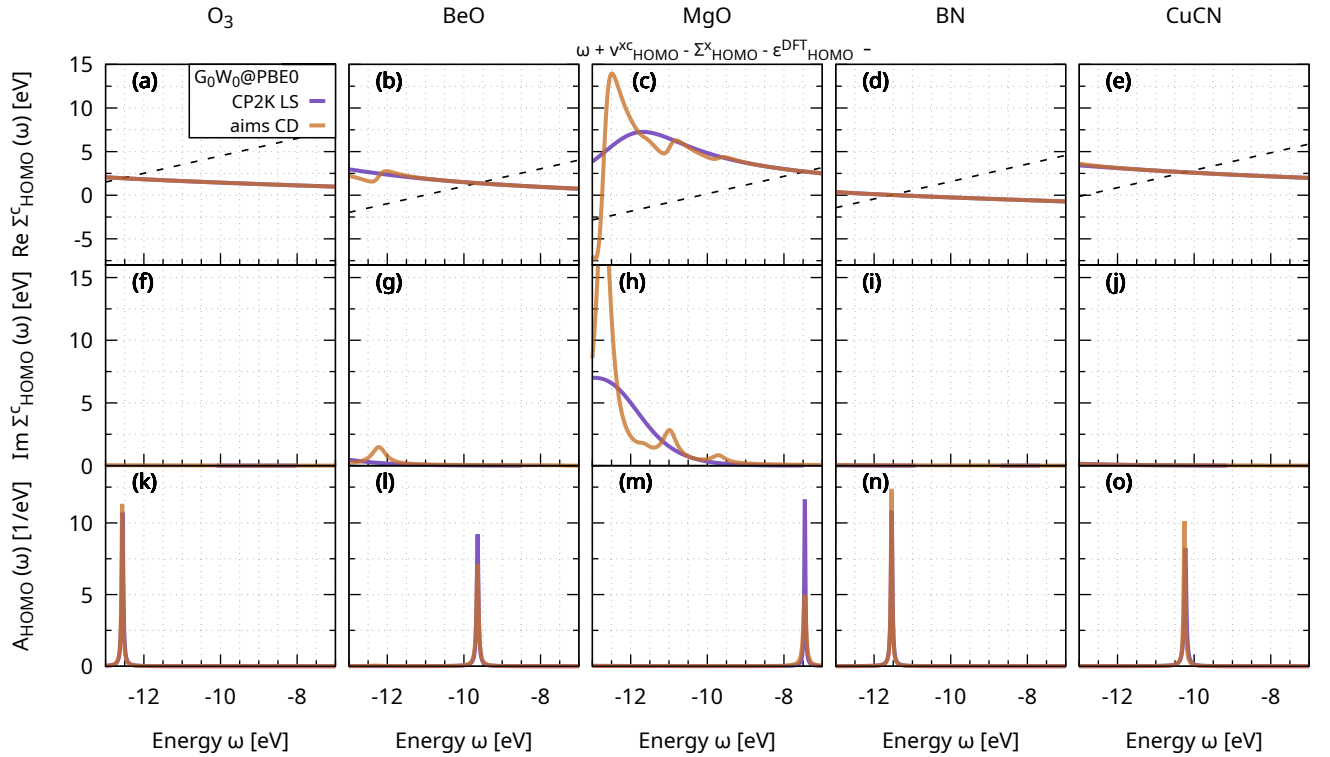


FIG. 8. (a)-(e)  $\text{Re}(\Sigma_{\text{HOMO}}^c)$ , (f)-(j)  $\text{Im}(\Sigma_{\text{HOMO}}^c)$ , (k)-(o)  $A_{\text{HOMO}}$  [Eq. (5)] for O<sub>3</sub>, BeO, MgO, BN and CuCN computed from G<sub>0</sub>W<sub>0</sub>@PBE0.

- [1] L. Hedin, New method for calculating the one-particle Green's function with application to the electron-gas problem, *Phys. Rev.* **139**, A796 (1965).
- [2] D. Golze, M. Dvorak, and P. Rinke, The GW Compendium: A Practical Guide to Theoretical Photoemission Spectroscopy, *Front. Chem.* **7**, 377 (2019).
- [3] L. Reining, The GW approximation: content, successes and limitations, *Wiley Interdiscip. Rev. Comput. Mol. Sci.* **8**, e1344 (2018).
- [4] X. Blase, C. Attaccalite, and V. Olevano, First-principles GW calculations for fullerenes, porphyrins, phthalocyanine, and other molecules of interest for organic photovoltaic applications, *Phys. Rev. B* **83**, 115103 (2011).
- [5] M. J. van Setten, F. Caruso, S. Sharifzadeh, X. Ren, M. Scheffler, F. Liu, J. Lischner, L. Lin, J. R. Deslippe, S. G. Louie, C. Yang, F. Weigend, J. B. Neaton, F. Evers, and P. Rinke, GW100: Benchmarking  $G_0W_0$  for Molecular Systems, *J. Chem. Theory Comput.* **11**, 5665 (2015).
- [6] J. W. Knight, X. Wang, L. Gallandi, O. Dolgounitcheva, X. Ren, J. V. Ortiz, P. Rinke, T. Körzdörfer, and N. Marom, Accurate Ionization Potentials and Electron Affinities of Acceptor Molecules III: A Benchmark of GW Methods, *J. Chem. Theory Comput.* **12**, 615 (2016).
- [7] A. Molina-Sánchez, D. Sangalli, K. Hummer, A. Marini, and L. Wirtz, Effect of spin-orbit interaction on the optical spectra of single-layer, double-layer, and bulk MoS<sub>2</sub>, *Phys. Rev. B* **88**, 045412 (2013).
- [8] W. Xia, W. Gao, G. Lopez-Candales, Y. Wu, W. Ren, W. Zhang, and P. Zhang, Combined subsampling and analytical integration for efficient large-scale GW calculations for 2D systems, *npj Comput. Mater.* **6**, 118 (2020).
- [9] M. N. Gjerding, A. Taghizadeh, A. Rasmussen, S. Ali, F. Bertoldo, T. Deilmann, N. R. Knøsgaard, M. Kruse, A. H. Larsen, S. Manti, T. G. Pedersen, U. Petralanda, T. Skovhus, M. K. Svendsen, J. J. Mortensen, T. Olsen, and K. S. Thygesen, Recent progress of the Computational 2D Materials Database (C2DB), *2D Mater.* **8**, 044002 (2021).
- [10] A. Rasmussen, T. Deilmann, and K. S. Thygesen, Towards fully automated GW band structure calculations: What we can learn from 60.000 self-energy evaluations, *npj Comput. Mater.* **7**, 22 (2021).
- [11] E. Mitterreiter, B. Schuler, A. Micevic, D. Hernangómez-Pérez, K. Barthelmi, K. A. Cochran, J. Kiemle, F. Sigger, J. Klein, E. Wong, E. S. Barnard, K. Watanabe, T. Taniguchi, M. Lorke, F. Jahnke, J. J. Finley, A. M. Schwartzberg, D. Y. Qiu, S. Refaely-Abramson, A. W. Holleitner, A. Weber-Bargioni, and C. Kastl, The role of chalcogen vacancies for atomic defect emission in MoS<sub>2</sub>, *Nat. Commun.* **12**, 3822 (2021).
- [12] K.-Q. Lin, C. S. Ong, S. Bange, P. E. Faria Junior, B. Peng, J. D. Ziegler, J. Zipfel, C. Bäuml, N. Paradiso, K. Watanabe, T. Taniguchi, C. Strunk, B. Monserrat, J. Fabian, A. Chernikov, D. Y. Qiu, S. G. Louie, and J. M. Lupton, Narrow-band high-lying excitons with negative-mass electrons in monolayer WSe<sub>2</sub>, *Nat. Commun.* **12**, 5500 (2021).
- [13] A. Guandalini, P. D'Amico, A. Ferretti, and D. Varsano, Efficient GW calculations in two dimensional materials through a stochastic integration of the screened potential, *npj Comput. Mater.* **9**, 44 (2023).
- [14] M. Graml, K. Zollner, D. Hernangómez-Pérez, P. E. Faria Junior, and J. Wilhelm, Low-Scaling GW Algorithm Applied to Twisted Transition-Metal Dichalcogenide Heterobilayers, *J. Chem. Theory Comput.* **20**, 2202 (2024).
- [15] M. Camarasa-Gómez, A. Ramasubramanian, J. B. Neaton, and L. Kronik, Transferable screened range-separated hybrid functionals for electronic and optical properties of van der Waals materials, *Phys. Rev. Mater.* **7**, 104001 (2023).
- [16] M. Camarasa-Gómez, S. E. Gant, G. Ohad, J. B. Neaton, A. Ramasubramanian, and L. Kronik, Electronic and Optical Excitations in van der Waals Materials from a Non-Empirical Wannier-Localized Optimally-Tuned Screened Range-Separated Hybrid Functional (2024), [arXiv:2405.00643](https://arxiv.org/abs/2405.00643).
- [17] R. Rodrigues Pela, C. Vona, S. Lubeck, B. Alex, I. Gonzalez Oliva, and C. Draxl, Critical assessment of  $G_0W_0$  calculations for 2D materials: the example of monolayer MoS<sub>2</sub>, *npj Comput. Mater.* **10**, 77 (2024).
- [18] J. Krumland and C. Cocchi, Electronic Structure of Low-Dimensional Inorganic/Organic Interfaces: Hybrid Density Functional Theory,  $G_0W_0$ , and Electrostatic Models, *Phys. Stat. Solidi A* **221**, 2300089 (2024).
- [19] J. Krumland and C. Cocchi, Ab Initio Modeling of Mixed-Dimensional Heterostructures: A Path Forward, *J. Phys. Chem. Lett.* **15**, 5350 (2024).
- [20] F. Bruneval and X. Gonze, Accurate GW self-energies in a plane-wave basis using only a few empty states: Towards large systems, *Phys. Rev. B* **78**, 085125 (2008).
- [21] M. R. Filip, G. E. Eperon, H. J. Snaith, and F. Giustino, Steric engineering of metal-halide perovskites with tunable optical band gaps, *Nat. Commun.* **5**, 5757 (2014).
- [22] Y. Cho and T. C. Berkelbach, Optical Properties of Layered Hybrid Organic-Inorganic Halide Perovskites: A Tight-Binding GW-BSE Study, *J. Phys. Chem. Lett.* **10**, 6189 (2019).
- [23] X. Ren, F. Merz, H. Jiang, Y. Yao, M. Rampp, H. Lederer, V. Blum, and M. Scheffler, All-electron periodic  $G_0W_0$  implementation with numerical atomic orbital basis functions: Algorithm and benchmarks, *Phys. Rev. Mater.* **5**, 013807 (2021).
- [24] R.-I. Biega, Y. Chen, M. R. Filip, and L. Leppert, Chemical Mapping of Excitons in Halide Double Perovskites, *Nano Lett.* **23**, 8155 (2023).
- [25] G. Biffi, Y. Cho, R. Krahne, and T. C. Berkelbach, Excitons and Their Fine Structure in Lead Halide Perovskite Nanocrystals from Atomistic GW/BSE Calculations, *J. Phys. Chem. C* **127**, 1891 (2023).
- [26] L. Leppert, Excitons in metal-halide perovskites from first-principles many-body perturbation theory, *J. Chem. Phys.* **160**, 050902 (2024).
- [27] D. Golze, J. Wilhelm, M. J. van Setten, and P. Rinke, Core-Level Binding Energies from GW: An Efficient Full-Frequency Approach within a Localized Basis., *J. Chem. Theory Comput.* **14**, 4856 (2018).
- [28] D. Golze, L. Keller, and P. Rinke, Accurate Absolute and Relative Core-Level Binding Energies from GW, *J. Phys. Chem. Lett.* **11**, 1840 (2020).
- [29] L. Keller, V. Blum, P. Rinke, and D. Golze, Relativistic correction scheme for core-level binding energies from GW, *J. Chem. Phys.* **153**, 114110 (2020).
- [30] T. Zhu and G. K.-L. Chan, All-Electron Gaussian-Based  $G_0W_0$  for Valence and Core Excitation Energies of Periodic Systems, *J. Chem. Theory Comput.* **17**, 727 (2021).

- [31] D. Mejia-Rodriguez, A. Kunitsa, E. Aprà, and N. Govind, Scalable Molecular GW Calculations: Valence and Core Spectra, *J. Chem. Theory Comput.* **17**, 7504 (2021).
- [32] D. Mejia-Rodriguez, A. Kunitsa, E. Aprà, and N. Govind, Basis Set Selection for Molecular Core-Level GW Calculations, *J. Chem. Theory Comput.* **18**, 4919 (2022).
- [33] J. Li, Y. Jin, P. Rinke, W. Yang, and D. Golze, Benchmark of GW Methods for Core-Level Binding Energies, *J. Chem. Theory Comput.* **18**, 7570 (2022).
- [34] R. L. Panadés-Barrueta and D. Golze, Accelerating Core-Level GW Calculations by Combining the Contour Deformation Approach with the Analytic Continuation of W, *J. Chem. Theory Comput.* **19**, 5450 (2023).
- [35] M. Kühn and F. Weigend, One-Electron Energies from the Two-Component GW Method, *J. Chem. Theory Comput.* **11**, 969 (2015).
- [36] C. Holzer and W. Klopper, Ionized, electron-attached, and excited states of molecular systems with spin-orbit coupling: Two-component GW and Bethe-Salpeter implementations, *J. Chem. Phys.* **150**, 204116 (2019).
- [37] C.-N. Yeh, A. Shee, Q. Sun, E. Gull, and D. Zgid, Relativistic self-consistent GW: Exact two-component formalism with one-electron approximation for solids, *Phys. Rev. B* **106**, 085121 (2022).
- [38] A. Förster, E. van Lenthe, E. Spadetto, and L. Visscher, Two-Component GW Calculations: Cubic Scaling Implementation and Comparison of Vertex-Corrected and Partially Self-Consistent GW Variants, *J. Chem. Theory Comput.* **19**, 5958 (2023).
- [39] M. Kehry, W. Klopper, and C. Holzer, Robust relativistic many-body Green's function based approaches for assessing core ionized and excited states, *J. Chem. Phys.* **159**, 044116 (2023).
- [40] H. Gaurav, A. Vibin, and D. Zgid, Challenges with relativistic GW calculations in solids and molecules, *Faraday Discuss.* (2024).
- [41] V. Abraham, G. Harsha, and D. Zgid, Relativistic fully self-consistent GW for molecules: Total energies and ionization potentials (2024), [arXiv:2401.11303](https://arxiv.org/abs/2401.11303).
- [42] O. Çaylak and B. Baumeier, Excited-State Geometry Optimization of Small Molecules with Many-Body Green's Functions Theory, *J. Chem. Theory Comput.* **17**, 879 (2021).
- [43] J. A. Berger, P.-F. Loos, and P. Romaniello, Potential Energy Surfaces without Unphysical Discontinuities: The Coulomb Hole Plus Screened Exchange Approach, *J. Chem. Theory Comput.* **17**, 191 (2021).
- [44] I. Knysh, K. Letellier, I. Duchemin, X. Blase, and D. Jacquemin, Excited state potential energy surfaces of n-phenylpyrrole upon twisting: reference values and comparison between bse/gw and td-dft, *Phys. Chem. Chem. Phys.* **25**, 8376 (2023).
- [45] I. Knysh, D. Raimbault, I. Duchemin, X. Blase, and D. Jacquemin, Assessing the accuracy of TD-DFT excited-state geometries through optimal tuning with GW energy levels, *J. Chem. Phys.* **160**, 144115 (2024).
- [46] C. Attaccalite, M. Grüning, and A. Marini, Real-time approach to the optical properties of solids and nanostructures: Time-dependent Bethe-Salpeter equation, *Phys. Rev. B* **84**, 245110 (2011).
- [47] X. Jiang, Q. Zheng, Z. Lan, W. A. Saidi, X. Ren, and J. Zhao, Real-time GW-BSE investigations on spin-valley exciton dynamics in monolayer transition metal dichalcogenide, *Sci. Adv.* **7**, eabf3759 (2021).
- [48] Y.-H. Chan, D. Y. Qiu, F. H. da Jornada, and S. G. Louie, Giant exciton-enhanced shift currents and direct current conduction with subbandgap photo excitations produced by many-electron interactions, *Proc. Natl. Acad. Sci. U.S.A.* **118**, e1906938118 (2021).
- [49] N. Schlünzen, J.-P. Joost, and M. Bonitz, Achieving the Scaling Limit for Nonequilibrium Green Functions Simulations, *Phys. Rev. Lett.* **124**, 076601 (2020).
- [50] J.-P. Joost, N. Schlünzen, and M. Bonitz, G1-G2 scheme: Dramatic acceleration of nonequilibrium Green functions simulations within the Hartree-Fock generalized Kadanoff-Baym ansatz, *Phys. Rev. B* **101**, 245101 (2020).
- [51] E. Perfetto, Y. Pavlyukh, and G. Stefanucci, Real-Time GW: Toward an Ab Initio Description of the Ultrafast Carrier and Exciton Dynamics in Two-Dimensional Materials, *Phys. Rev. Lett.* **128**, 016801 (2022).
- [52] R. Tuovinen, D. Golež, M. Eckstein, and M. A. Sentef, Comparing the generalized Kadanoff-Baym ansatz with the full Kadanoff-Baym equations for an excitonic insulator out of equilibrium, *Phys. Rev. B* **102**, 115157 (2020).
- [53] R. Tuovinen, R. van Leeuwen, E. Perfetto, and G. Stefanucci, Electronic transport in molecular junctions: The generalized Kadanoff-Baym ansatz with initial contact and correlations, *J. Chem. Phys.* **154**, 094104 (2021).
- [54] R. Tuovinen, Y. Pavlyukh, E. Perfetto, and G. Stefanucci, Time-Linear Quantum Transport Simulations with Correlated Nonequilibrium Green's Functions, *Phys. Rev. Lett.* **130**, 246301 (2023).
- [55] Y. Pavlyukh, R. Tuovinen, E. Perfetto, and G. Stefanucci, Cheers: A Linear-Scaling KBE+GKBA Code, *Phys. Status Solidi B*, 2300504 (2023).
- [56] M. Bonitz, J.-P. Joost, C. Makait, E. Schroedter, T. Kalsberger, and K. Balzer, Accelerating Nonequilibrium Green Functions Simulations: The G1-G2 Scheme and Beyond, *Phys. Status Solidi B*, 2300578 (2024).
- [57] C. C. Reeves, G. Harsha, A. Shee, Y. Zhu, C. Yang, K. B. Whaley, D. Zgid, and V. Vlcek, Performance of wave function and Green's functions based methods for non equilibrium many-body dynamics (2024), [arXiv:2405.08814](https://arxiv.org/abs/2405.08814).
- [58] C. Holzer, A. M. Teale, F. Hampe, S. Stopkowitz, T. Helgaker, and W. Klopper, GW quasiparticle energies of atoms in strong magnetic fields, *J. Chem. Phys.* **150**, 214112 (2019).
- [59] C. Holzer, A. Pausch, and W. Klopper, The GW/BSE method in magnetic fields, *Front. Chem.* **9**, 746162 (2021).
- [60] Y. J. Franzke, C. Holzer, and F. Mack, NMR Coupling Constants Based on the Bethe-Salpeter Equation in the GW Approximation, *J. Chem. Theory Comput.* **18**, 1030 (2022).
- [61] C. Holzer, Practical Post-Kohn-Sham Methods for Time-Reversal Symmetry Breaking References, *J. Chem. Theory Comput.* **19**, 3131 (2023).
- [62] F. Bruneval, N. Dattani, and M. J. van Setten, The GW Miracle in Many-Body Perturbation Theory for the Ionization Potential of Molecules, *Front. Chem.* **9**, 749779 (2021).
- [63] R. Orlando, P. Romaniello, and P.-F. Loos, The three channels of many-body perturbation theory: GW, particle-particle, and electron-hole T-matrix self-energies, *J. Chem. Phys.* **159**, 184113 (2023).
- [64] S. Marek and R. Korytár, Widening of the fundamental gap in cluster gw for metal-molecular interfaces, *Phys. Chem. Chem. Phys.* **26**, 2127 (2024).
- [65] A. Ammar, A. Marie, M. Rodríguez-Mayorga, H. G. A. Burton, and P.-F. Loos, Can GW Handle Multireference Systems? (2024), [arXiv:2401.03745](https://arxiv.org/abs/2401.03745).

- [66] E. Maggio, P. Liu, M. J. van Setten, and G. Kresse, GW100: A Plane Wave Perspective for Small Molecules, *J. Chem. Theory Comput.* **13**, 635 (2017).
- [67] M. J. van Setten, M. Giantomassi, X. Gonze, G.-M. Rignanese, and G. Hautier, Automation methodologies and large-scale validation for GW: Towards high-throughput GW calculations, *Phys. Rev. B* **96**, 155207 (2017).
- [68] W. Gao and J. R. Chelikowsky, Real-Space Based Benchmark of  $G_0W_0$  Calculations on GW100: Effects of Semicore Orbitals and Orbital Reordering, *J. Chem. Theory Comput.* **15**, 5299 (2019).
- [69] M. Govoni and G. Galli, GW100: Comparison of Methods and Accuracy of Results Obtained with the WEST Code, *J. Chem. Theory Comput.* **14**, 1895 (2018).
- [70] A. Förster and L. Visscher, GW100: A Slater-Type Orbital Perspective, *J. Chem. Theory Comput.* **17**, 5080 (2021).
- [71] T. Rangel, M. Del Ben, D. Varsano, G. Antonius, F. Bruneval, F. H. da Jornada, M. J. van Setten, O. K. Orhan, D. D. O'Regan, A. Canning, A. Ferretti, A. Marini, G.-M. Rignanese, J. Deslippe, S. G. Louie, and J. B. Neaton, Reproducibility in  $g_0w_0$  calculations for solids, *Comput. Phys. Commun.* **255**, 107242 (2020).
- [72] A. Stuke, C. Kunkel, D. Golze, M. Todorović, J. T. Margraf, K. Reuter, P. Rinke, and H. Oberhofer, Atomic structures and orbital energies of 61,489 crystal-forming organic molecules, *Sci. Data* **7**, 1 (2020).
- [73] J. Westermayr and R. J. Maurer, Physically inspired deep learning of molecular excitations and photoemission spectra, *Chem. Sci.* **12**, 10755 (2021).
- [74] D. Golze, M. Hirvensalo, P. Hernández-León, A. Aarva, J. Etula, T. Susi, P. Rinke, T. Laurila, and M. A. Caro, Accurate Computational Prediction of Core-Electron Binding Energies in Carbon-Based Materials: A Machine-Learning Model Combining Density-Functional Theory and GW, *Chem. Mater.* **34**, 6240 (2022).
- [75] A. Fediai, P. Reiser, J. E. O. Peña, W. Wenzel, and P. Friederich, Interpretable delta-learning of GW quasiparticle energies from GGA-DFT, *Mach. Learn. Sci. Technol.* **4**, 035045 (2023).
- [76] B. Mondal, J. Westermayr, and R. Tonner-Zech, Machine learning for accelerated bandgap prediction in strain-engineered quaternary III-V semiconductors, *J. Chem. Phys.* **159**, 104702 (2023).
- [77] M. G. Zauchner, A. Horsfield, and J. Lischner, Accelerating GW calculations through machine-learned dielectric matrices, *npj Comput. Mater.* **9**, 184 (2023).
- [78] C. Venturella, C. Hillenbrand, J. Li, and T. Zhu, Machine Learning Many-Body Green's Functions for Molecular Excitation Spectra, *J. Chem. Theory Comput.* **20**, 143 (2024).
- [79] R. Del Sole, L. Reining, and R. W. Godby,  $GW\Gamma$  approximation for electron self-energies in semiconductors and insulators, *Phys. Rev. B* **49**, 8024 (1994).
- [80] E. L. Shirley and R. M. Martin, GW quasiparticle calculations in atoms, *Phys. Rev. B* **47**, 15404 (1993).
- [81] F. Bruneval, F. Sottile, V. Olevano, R. Del Sole, and L. Reining, Many-Body Perturbation Theory Using the Density-Functional Concept: Beyond the GW Approximation, *Phys. Rev. Lett.* **94**, 186402 (2005).
- [82] M. Shishkin, M. Marsman, and G. Kresse, Accurate Quasiparticle Spectra from Self-Consistent GW Calculations with Vertex Corrections, *Phys. Rev. Lett.* **99**, 246403 (2007).
- [83] A. Grüneis, G. Kresse, Y. Hinuma, and F. Oba, Ionization Potentials of Solids: The Importance of Vertex Corrections, *Phys. Rev. Lett.* **112**, 096401 (2014).
- [84] E. Maggio and G. Kresse, GW Vertex Corrected Calculations for Molecular Systems, *J. Chem. Theory Comput.* **13**, 4765 (2017).
- [85] A. M. Lewis and T. C. Berkelbach, Vertex Corrections to the Polarizability Do Not Improve the GW Approximation for the Ionization Potential of Molecules, *J. Chem. Theory Comput.* **15**, 2925 (2019).
- [86] A. Tal, W. Chen, and A. Pasquarello, Vertex function compliant with the Ward identity for quasiparticle self-consistent calculations beyond GW, *Phys. Rev. B* **103**, L161104 (2021).
- [87] Y. Wang, P. Rinke, and X. Ren, Assessing the  $G_0W_0\Gamma_0^{(1)}$  Approach: Beyond  $G_0W_0$  with Hedin's Full Second-Order Self-Energy Contribution, *J. Chem. Theory Comput.* **17**, 5140 (2021).
- [88] A. Förster and L. Visscher, Exploring the statically screened  $G_3W_2$  correction to the GW self-energy: Charged excitations and total energies of finite systems, *Phys. Rev. B* **105**, 125121 (2022).
- [89] A. Lorin, T. Bischoff, A. Tal, and A. Pasquarello, Band alignments through quasiparticle self-consistent GW with efficient vertex corrections, *Phys. Rev. B* **108**, 245303 (2023).
- [90] F. Bruneval and A. Förster, Fully Dynamic  $G_3W_2$  Self-Energy for Finite Systems: Formulas and Benchmark, *J. Chem. Theory Comput.* **20**, 3218 (2024).
- [91] M. Wen, V. Abraham, G. Harsha, A. Shee, K. B. Whaley, and D. Zgid, Comparing Self-Consistent GW and Vertex-Corrected  $G_0W_0$  ( $G_0W_0\Gamma$ ) Accuracy for Molecular Ionization Potentials, *J. Chem. Theory Comput.* **20**, 3109 (2024).
- [92] M. F. Lange and T. C. Berkelbach, On the Relation between Equation-of-Motion Coupled-Cluster Theory and the GW Approximation, *J. Chem. Theory Comput.* **14**, 4224 (2018).
- [93] J. Tölle and G. Kin-Lic Chan, Exact relationships between the GW approximation and equation-of-motion coupled-cluster theories through the quasi-boson formalism, *J. Chem. Phys.* **158**, 124123 (2023).
- [94] J. Tölle and G. Kin-Lic Chan, AB- $G_0W_0$ : A practical  $G_0W_0$  method without frequency integration based on an auxiliary boson expansion, *J. Chem. Phys.* **160**, 164108 (2024).
- [95] J. McClain, Q. Sun, G. K.-L. Chan, and T. C. Berkelbach, Gaussian-Based Coupled-Cluster Theory for the Ground-State and Band Structure of Solids, *J. Chem. Theory Comput.* **13**, 1209 (2017).
- [96] X. Wang and T. C. Berkelbach, Excitons in Solids from Periodic Equation-of-Motion Coupled-Cluster Theory, *J. Chem. Theory Comput.* **16**, 3095 (2020).
- [97] X. Wang and T. C. Berkelbach, Absorption Spectra of Solids from Periodic Equation-of-Motion Coupled-Cluster Theory, *J. Chem. Theory Comput.* **17**, 6387 (2021).
- [98] K. Laughon, J. M. Yu, and T. Zhu, Periodic Coupled-Cluster Green's Function for Photoemission Spectra of Realistic Solids, *J. Phys. Chem. Lett.* **13**, 9122 (2022).
- [99] A. Gallo, F. Hummel, A. Irmmler, and A. Grüneis, A periodic equation-of-motion coupled-cluster implementation applied to F-centers in alkaline earth oxides, *J. Chem. Phys.* **154**, 064106 (2021).
- [100] N. Masios, A. Irmmler, T. Schäfer, and A. Grüneis, Averting the Infrared Catastrophe in the Gold Standard of Quantum Chemistry, *Phys. Rev. Lett.* **131**, 186401 (2023).
- [101] P. J. Robinson, A. Rettig, H. Q. Dinh, M.-F. Chen, and J. Lee, Condensed-Phase Quantum Chemistry (2024), [arXiv:2403.13207](https://arxiv.org/abs/2403.13207).
- [102] F. Fuchs, C. Rödl, A. Schleife, and F. Bechstedt, Efficient  $\mathcal{O}(N^2)$  approach to solve the Bethe-Salpeter equation for ex-

- citonic bound states, *Phys. Rev. B* **78**, 085103 (2008).
- [103] X. Blase, I. Duchemin, D. Jacquemin, and P.-F. Loos, The Bethe–Salpeter Equation Formalism: From Physics to Chemistry, *J. Phys. Chem. Lett.* **11**, 7371 (2020).
- [104] K. Merkel and F. Ortman, Linear scaling approach for optical excitations using maximally localized Wannier functions, *J. Phys. Mater.* **7**, 015001 (2023).
- [105] M. Govoni and G. Galli, Large Scale GW Calculations, *J. Chem. Theory Comput.* **11**, 2680 (2015).
- [106] M. Kim, S. Mandal, E. Mikida, K. Chandrasekar, E. Bohm, N. Jain, Q. Li, R. Kanakagiri, G. J. Martyna, L. Kale, and S. Ismail-Beigi, Scalable GW software for quasiparticle properties using OpenAtom, *Comput. Phys. Commun.* **244**, 427 (2019).
- [107] D. Sangalli, A. Ferretti, H. Miranda, C. Attaccalite, I. Marri, E. Cannuccia, P. Melo, M. Marsili, F. Paleari, A. Marrazzo, G. Prandini, P. Bonfà, M. O. Atambo, F. Affinito, M. Palumbo, A. Molina-Sánchez, C. Hogan, M. Grüning, D. Varsano, and A. Marini, Many-body perturbation theory calculations using the yambo code, *J. Phys. Condens. Matter* **31**, 325902 (2019).
- [108] M. Del Ben, H. Felipe, A. Canning, N. Wichmann, K. Raman, R. Sasanka, C. Yang, S. G. Louie, and J. Deslippe, Large-scale GW calculations on pre-exascale HPC systems, *Comput. Phys. Commun.* **235**, 187 (2019).
- [109] M. D. Ben, C. Yang, Z. Li, F. H. d. Jornada, S. G. Louie, and J. Deslippe, Accelerating Large-Scale Excited-State GW Calculations on Leadership HPC Systems, in *SC20: International Conference for High Performance Computing, Networking, Storage and Analysis* (2020) pp. 1–11.
- [110] V. W.-z. Yu and M. Govoni, GPU Acceleration of Large-Scale Full-Frequency GW Calculations, *J. Chem. Theory Comput.* **18**, 4690 (2022).
- [111] C.-N. Yeh, S. Isakov, D. Zgid, and E. Gull, Fully self-consistent finite-temperature GW in Gaussian Bloch orbitals for solids, *Phys. Rev. B* **106**, 235104 (2022).
- [112] I. Duchemin, D. Jacquemin, and X. Blase, Combining the gw formalism with the polarizable continuum model: A state-specific non-equilibrium approach, *J. Chem. Phys.* **144**, 164106 (2016).
- [113] J. Li, G. D’Avino, I. Duchemin, D. Beljonne, and X. Blase, Combining the Many-Body GW Formalism with Classical Polarizable Models: Insights on the Electronic Structure of Molecular Solids, *J. Phys. Chem. Lett.* **7**, 2814 (2016).
- [114] J. Li, G. D’Avino, I. Duchemin, D. Beljonne, and X. Blase, Accurate description of charged excitations in molecular solids from embedded many-body perturbation theory, *Phys. Rev. B* **97**, 035108 (2018).
- [115] J. Tölle, T. Deilmann, M. Rohlfing, and J. Neugebauer, Subsystem-Based GW/Bethe–Salpeter Equation, *J. Chem. Theory Comput.* **17**, 2186 (2021).
- [116] D. Amblard, X. Blase, and I. Duchemin, Many-body GW calculations with very large scale polarizable environments made affordable: A fully ab-initio QM/QM approach, *J. Chem. Phys.* **159**, 164107 (2023).
- [117] D. Amblard, X. Blase, and I. Duchemin, Static versus dynamically polarizable environments within the many-body GW formalism, *J. Chem. Phys.* **160**, 154104 (2024).
- [118] H. N. Rojas, R. W. Godby, and R. J. Needs, Space-Time Method for Ab Initio Calculations of Self-Energies and Dielectric Response Functions of Solids, *Phys. Rev. Lett.* **74**, 1827 (1995).
- [119] D. Foerster, P. Koval, and D. Sánchez-Portal, An  $O(N^3)$  implementation of Hedin’s GW approximation for molecules, *J. Chem. Phys.* **135**, 074105 (2011).
- [120] D. Neuhauser, Y. Gao, C. Arntsen, C. Karshenas, E. Rabani, and R. Baer, Breaking the Theoretical Scaling Limit for Predicting Quasiparticle Energies: The Stochastic GW Approach, *Phys. Rev. Lett.* **113**, 076402 (2014).
- [121] P. Liu, M. Kaltak, J. Klimeš, and G. Kresse, Cubic scaling GW: Towards fast quasiparticle calculations, *Phys. Rev. B* **94**, 165109 (2016).
- [122] W. Gao and J. R. Chelikowsky, Accelerating Time-Dependent Density Functional Theory and GW Calculations for Molecules and Nanoclusters with Symmetry Adapted Interpolative Separable Density Fitting, *J. Chem. Theory Comput.* **16**, 2216 (2020).
- [123] J. Wilhelm, D. Golze, L. Talirz, J. Hutter, and C. A. Pignedoli, Toward GW Calculations on Thousands of Atoms, *J. Phys. Chem. Lett.* **9**, 306–312 (2018).
- [124] I. Duchemin and X. Blase, Separable resolution-of-the-identity with all-electron Gaussian bases: Application to cubic-scaling RPA, *J. Chem. Phys.* **150**, 174120 (2019).
- [125] A. Förster and L. Visscher, Low-Order Scaling  $G_0W_0$  by Pair Atomic Density Fitting, *J. Chem. Theory Comput.* **16**, 7381–7399 (2020).
- [126] M. Kim, G. J. Martyna, and S. Ismail-Beigi, Complex-time shredded propagator method for large-scale GW calculations, *Phys. Rev. B* **101**, 035139 (2020).
- [127] A. L. Kutepov, Self-consistent GW method:  $O(N)$  algorithm for polarizability and self energy, *Comput. Phys. Commun.* **257**, 107502 (2020).
- [128] W. Gao, W. Xia, P. Zhang, J. R. Chelikowsky, and J. Zhao, Numerical methods for efficient GW calculations and the applications in low-dimensional systems, *Electron. Struct.* **4**, 023003 (2022).
- [129] J. Wilhelm, P. Seewald, and D. Golze, Low-Scaling GW with Benchmark Accuracy and Application to Phosphorene Nanosheets, *J. Chem. Theory Comput.* **17**, 1662 (2021).
- [130] C.-N. Yeh and M. A. Morales, Low-Scaling Algorithms for GW and Constrained Random Phase Approximation Using Symmetry-Adapted Interpolative Separable Density Fitting, *J. Chem. Theory Comput.* **20**, 3184 (2024).
- [131] R. Shi, P. Lin, M.-Y. Zhang, L. He, and X. Ren, Subquadratic-scaling real-space random phase approximation correlation energy calculations for periodic systems with numerical atomic orbitals, *Phys. Rev. B* **109**, 035103 (2024).
- [132] A. Förster and L. Visscher, Low-order scaling quasiparticle self-consistent GW for molecules, *Front. Chem.* **9**, 736591 (2021).
- [133] A. Förster and L. Visscher, Quasiparticle Self-Consistent GW-Bethe–Salpeter Equation Calculations for Large Chromophoric Systems, *J. Chem. Theory Comput.* **18**, 6779 (2022).
- [134] E. Spadetto, P. H. T. Philipsen, A. Forster, and L. Visscher, Toward Pair Atomic Density Fitting for Correlation Energies with Benchmark Accuracy, *J. Chem. Theory Comput.* **19**, 1499 (2023).
- [135] D. Golze, M. Iannuzzi, and J. Hutter, Local Fitting of the Kohn–Sham Density in a Gaussian and Plane Waves Scheme for Large-Scale Density Functional Theory Simulations, *J. Chem. Theory Comput.* **13**, 2202 (2017).
- [136] J. Lu and L. Ying, Compression of the electron repulsion integral tensor in tensor hypercontraction format with cubic scaling cost, *J. Comput. Phys.* **302**, 329 (2015).
- [137] J. Lu and K. Thicke, Cubic scaling algorithms for RPA correlation using interpolative separable density fitting, *J. Comput. Phys.* **351**, 187 (2017).

- [138] I. Duchemin and X. Blase, Cubic-Scaling All-Electron GW Calculations with a Separable Density-Fitting Space-Time Approach, *J. Chem. Theory Comput.* **17**, 2383 (2021).
- [139] F. A. Delesma, M. Leucke, D. Golze, and P. Rinke, Benchmarking the accuracy of the separable resolution of the identity approach for correlated methods in the numeric atom-centered orbitals framework, *J. Chem. Phys.* **160**, 024118 (2024).
- [140] W. Gao, Z. Tang, J. Zhao, and J. R. Chelikowsky, Efficient Full-Frequency GW Calculations Using a Lanczos Method, *Phys. Rev. Lett.* **132**, 126402 (2024).
- [141] O. Vahtras, J. Almlöf, and M. Feyereisen, Integral approximations for LCAO-SCF calculations, *Chem. Phys. Lett.* **213**, 514 (1993).
- [142] Y. Jung, A. Sodt, P. M. Gill, and M. Head-Gordon, Auxiliary basis expansions for large-scale electronic structure calculations, *Proc. Natl. Acad. Sci. U.S.A.* **102**, 6692 (2005).
- [143] M. Azizi, J. Wilhelm, D. Golze, M. Giantomassi, R. L. Panadés-Barrueta, F. A. Delesma, A. Buccheri, A. Gulans, P. Rinke, C. Draxl, and X. Gonze, Time-frequency component of the GreenX library: minimax grids for efficient RPA and GW calculations, *J. Open Source Softw.* **8**, 5570 (2023).
- [144] M. Azizi, J. Wilhelm, D. Golze, F. A. Delesma, R. L. Panadés-Barrueta, P. Rinke, M. Giantomassi, and X. Gonze, Validation of the GreenX library time-frequency component for efficient GW and RPA calculations (2024), [arXiv:2403.06709](https://arxiv.org/abs/2403.06709).
- [145] J. Tölle, N. Niemeyer, and J. Neugebauer, Accelerating Analytic-Continuation GW Calculations with a Laplace Transform and Natural Auxiliary Functions, *J. Chem. Theory Comput.* **20**, 2022 (2024).
- [146] J. P. Perdew, K. Burke, and M. Ernzerhof, Generalized Gradient Approximation Made Simple, *Phys. Rev. Lett.* **77**, 3865 (1996).
- [147] W. Kohn and L. J. Sham, Self-Consistent Equations Including Exchange and Correlation Effects, *Phys. Rev.* **140**, A1133 (1965).
- [148] F. Caruso, M. Dauth, M. J. van Setten, and P. Rinke, Benchmark of GW Approaches for the GW100 Test Set, *J. Chem. Theory Comput.* **12**, 5076–5087 (2016).
- [149] S. J. Bintrim and T. C. Berkelbach, Full-frequency GW without frequency, *J. Chem. Phys.* **154**, 041101 (2021).
- [150] C. J. C. Scott, O. J. Backhouse, and G. H. Booth, A “moment-conserving” reformulation of GW theory, *J. Chem. Phys.* **158**, 124102 (2023).
- [151] E. Monino and P.-F. Loos, Connections and performances of Green’s function methods for charged and neutral excitations, *J. Chem. Phys.* **159**, 034105 (2023).
- [152] I. Duchemin and X. Blase, Robust Analytic-Continuation Approach to Many-Body GW Calculations, *J. Chem. Theory Comput.* **16**, 1742 (2020).
- [153] W. Gao and J. R. Chelikowsky, Real-Space Based Benchmark of  $G_0W_0$  Calculations on GW100: Effects of Semicore Orbitals and Orbital Reordering, *J. Chem. Theory Comput.* **15**, 5299 (2019).
- [154] M. J. van Setten, F. Weigend, and F. Evers, The GW-method for quantum chemistry applications: Theory and implementation, *J. Chem. Theory Comput.* **9**, 232 (2013).
- [155] C. A. Ullrich, *Time-Dependent Density-Functional Theory: Concepts and Applications* (Oxford University Press, 2011).
- [156] G. Onida, L. Reining, and A. Rubio, Electronic excitations: density-functional versus many-body Green’s-function approaches, *Rev. Mod. Phys.* **74**, 601 (2002).
- [157] A. Marie, A. Ammar, and P.-F. Loos, *The GW Approximation: A Quantum Chemistry Perspective* (2024), [arXiv:2311.05351](https://arxiv.org/abs/2311.05351).
- [158] H. J. Vidberg and J. W. Serene, Solving the Eliashberg equations by means of N-point Padé approximants, *J. Low Temp. Phys.* **29**, 179 (1977).
- [159] S. L. Adler, Quantum theory of the dielectric constant in real solids, *Phys. Rev.* **126**, 413 (1962).
- [160] N. Wiser, Dielectric constant with local field effects included, *Phys. Rev.* **129**, 62 (1963).
- [161] R. W. Godby, M. Schlüter, and L. J. Sham, Self-energy operators and exchange-correlation potentials in semiconductors, *Phys. Rev. B* **37**, 10159 (1988).
- [162] S. Lebègue, M. Klintonberg, O. Eriksson, and M. I. Katsnelson, Accurate electronic band gap of pure and functionalized graphane from GW calculations, *Phys. Rev. B* **79**, 245117 (2009).
- [163] X. Gonze, B. Amadon, P.-M. Anglade, J.-M. Beuken, F. Bottin, P. Boulanger, F. Bruneval, D. Caliste, R. Caracas, M. Côté, T. Deutsch, L. Genovese, P. Ghosez, M. Giantomassi, S. Goedecker, D. Hamann, P. Hermet, F. Jollet, G. Jomard, S. Leroux, M. Mancini, S. Mazevet, M. Oliveira, G. Onida, Y. Pouillon, T. Rangel, G.-M. Rignanese, D. Sangalli, R. Shaltaf, M. Torrent, M. Verstraete, G. Zerah, and J. Zwanziger, ABINIT: First-principles approach to material and nanosystem properties, *Comput. Phys. Commun.* **180**, 2582 (2009).
- [164] T. D. Kühne, M. Iannuzzi, M. Del Ben, V. V. Rybkin, P. Seewald, F. Stein, T. Laino, R. Z. Khaliullin, O. Schütt, F. Schiffmann, D. Golze, J. Wilhelm, S. Chulkov, M. H. Bani-Hashemian, V. Weber, U. Borštnik, M. Taillefumier, A. S. Jakobovits, A. Lazzaro, H. Pabst, T. Müller, R. Schade, M. Guidon, S. Andermatt, N. Holmberg, G. K. Schenter, A. Hehn, A. Bussy, F. Belleflamme, G. Tabacchi, A. Glöb, M. Lass, I. Bethune, C. J. Mundy, C. Plessl, M. Watkins, J. VandeVondele, M. Krack, and J. Hutter, CP2K: An electronic structure and molecular dynamics software package - Quickstep: Efficient and accurate electronic structure calculations, *J. Chem. Phys.* **152**, 194103 (2020).
- [165] CP2K, <https://www.cp2k.org>, <https://github.com/cp2k/cp2k> (accessed 15 March 2024).
- [166] G. Lippert, J. Hutter, and M. Parrinello, The Gaussian and augmented-plane-wave density functional method for ab initio molecular dynamics simulations, *Theor. Chem. Acc.* **103**, 124 (1999).
- [167] F. Weigend, F. Furche, and R. Ahlrichs, Gaussian basis sets of quadruple zeta valence quality for atoms H–Kr, *J. Chem. Phys.* **119**, 12753 (2003).
- [168] C. Hättig, Optimization of auxiliary basis sets for ri-mp2 and ri-cc2 calculations: Core–valence and quintuple- $\zeta$  basis sets for h to ar and qzvpv basis sets for li to kr, *Phys. Chem. Chem. Phys.* **7**, 59 (2005).
- [169] M. Kaltak, J. Klimes, and G. Kresse, Low Scaling Algorithms for the Random Phase Approximation: Imaginary Time and Laplace Transformations, *J. Chem. Theory Comput.* **10**, 2498 (2014).
- [170] D. Golze, N. Benedikter, M. Iannuzzi, J. Wilhelm, and J. Hutter, Fast evaluation of solid harmonic Gaussian integrals for local resolution-of-the-identity methods and range-separated hybrid functionals, *J. Chem. Phys.* **146**, 034105 (2017).
- [171] E. F. Valeev, Libint, A library for the evaluation of molecular integrals of operators over Gaussian functions, <https://github.com/evaleev/libint> (accessed 15 March 2024).
- [172] V. Blum, R. Gehrke, F. Hanke, P. Havu, V. Havu, X. Ren, K. Reuter, and M. Scheffler, Ab initio molecular simulations with numeric atom-centered orbitals, *Comput. Phys. Commun.* **180**, 2175 (2009).



- [173] X. Ren, P. Rinke, V. Blum, J. Wieferink, A. Tkatchenko, A. Sanfilippo, K. Reuter, and M. Scheffler, Resolution-of-identity approach to Hartree–Fock, hybrid density functionals, RPA, MP2 and *GW* with numeric atom-centered orbital basis functions, *New J. Phys.* **14**, 053020 (2012).
- [174] A. Takatsuka, S. Ten-no, and W. Hackbusch, Minimax approximation for the decomposition of energy denominators in Laplace-transformed Møller–Plesset perturbation theories, *J. Chem. Phys.* **129**, 044112 (2008).
- [175] M. Del Ben, O. Schütt, T. Wentz, P. Messmer, J. Hutter, and J. VandeVondele, Enabling simulation at the fifth rung of DFT: Large scale RPA calculations with excellent time to solution, *Comput. Phys. Commun.* **187**, 120 (2015).
- [176] B. Helmich-Paris and L. Visscher, Improvements on the minimax algorithm for the Laplace transformation of orbital energy denominators, *J. Comput. Phys.* **321**, 927 (2016).
- [177] W. Hackbusch, Computation of best  $L^\infty$  exponential sums for  $1/x$  by Remez’ algorithm, *Comput. Vis. Sci.* **20**, 1 (2019).
- [178] M. Häser and J. Almlöf, Laplace transform techniques in Møller–Plesset perturbation theory, *J. Chem. Phys.* **96**, 489 (1992).
- [179] P. Y. Ayala and G. E. Scuseria, Linear scaling second-order Møller–Plesset theory in the atomic orbital basis for large molecular systems, *J. Chem. Phys.* **110**, 3660 (1999).
- [180] D. S. Lambrecht, B. Doser, and C. Ochsenfeld, Rigorous integral screening for electron correlation methods, *J. Chem. Phys.* **123**, 184102 (2005).
- [181] D. Kats, D. Usvyat, and M. Schütz, On the use of the Laplace transform in local correlation methods, *Phys. Chem. Chem. Phys.* **10**, 3430 (2008).
- [182] D. Kats, D. Usvyat, S. Loibl, T. Merz, and M. Schütz, Comment on “Minimax approximation for the decomposition of energy denominators in Laplace-transformed Møller–Plesset perturbation theories” [J. Chem. Phys. 129, 044112 (2008)], *J. Chem. Phys.* **130**, 127101 (2009).
- [183] GreenX, <https://github.com/nomad-coe/greenX> (accessed 15 March 2024).
- [184] T. J. Pollehn, A. Schindlmayr, and R. W. Godby, Assessment of the *GW* approximation using Hubbard chains, *J. Phys. Condens. Matter* **10**, 1273 (1998).
- [185] M. Schambeck, NOMAD repository *GW* calculations on  $O_3$ ,  $BeO$ ,  $MgO$ ,  $BN$ ,  $CuCN$  (2024).
- [186] M. Schambeck, [https://github.com/miasb/GW\\_calculations\\_03\\_BeO\\_MgO\\_BN\\_CuCN](https://github.com/miasb/GW_calculations_03_BeO_MgO_BN_CuCN) (accessed 28 May 2024).